

Large-Eddy Simulation of a Wind Turbine Using a Filtered Actuator Line Model

Ronith Stanly^a, Luis A. Martínez-Tossas^b, Steven H. Frankel^a, Yann Delorme^a

^a*Technion - Israel Institute of Technology, Haifa, Israel*

^b*National Renewable Energy Laboratory, Golden, Colorado, USA*

Abstract

When dealing with multirotor devices such as quadcopters or wind farms, the cost of blade-resolved large-eddy simulation (LES) becomes prohibitive. Combining LES with a family of lower-fidelity models, called actuator line models (ALMs), has grown in popularity in the past decade. ALM replaces full blade resolution with an array of actuator points or lines parameterized by aerodynamic lift/drag polar plots along the blades. Body forces computed based on these actuator points are then projected onto the LES flow mesh, mimicking the effect of rotating blades on the flow. However, the optimal projection radius and the associated LES grid size is often too restrictive for multirotor simulations. Recently, a new tip-correction-based filtered ALM (F-ALM) was proposed by Martínez-Tossas and Meneveau (2019), which allows coarser-than-optimal grids by avoiding the associated overprediction of thrust. In this work, F-ALM is implemented into a high-order, in-house LES code to simulate National Renewable Energy Laboratory Phase VI wind turbine. It is then followed by a comparison between the baseline ALM and the newly implemented F-ALM in terms of instantaneous and time-averaged flow fields and blade loads, revealing the advantages of F-ALM in preventing the overprediction of power on coarse grids. This encourages accurate and affordable simulations of multirotor devices in the future.

Keywords: Actuator Line Model, Parallel, Coarse Grid, Wind Turbine, NREL Phase VI Rotor

1. Introduction

Engineering devices employing rotors¹ such as propellers (Caprace et al., 2017, 2020, 2021) on unmanned urban vehicles (Delorme et al., 2020; Stanly et al., 2020) and wind (Korobenko et al., 2017; Benard et al., 2018; Yan et al., 2016), hydrokinetic (Mohamed et al., 2020) and tidal turbines (Ouro and Stoesser, 2017; Yan et al., 2017) play a vital role in both propulsion and energy extraction. These devices operate in atmospheric turbulence (Porté-Agel et al., 2011; Dörenkämper et al., 2015; Richards and Norris, 2019, 2011, 2015; Bouras et al., 2018; Vasurato et al., 2018), feature complex unsteady turbulent flow fields (Troldborg et al., 2014, 2015b, 2011; Önder and Meyers, 2018; Rocchio et al., 2020; Storey et al., 2014) and have significant non-local effects related to downstream wake interactions (Kleusberg et al., 2020; Kleusberg, 2019; Kleusberg et al., 2017a; Sarmast et al., 2014a,b; Kleusberg et al., 2016; Ciri et al., 2020; Ivanell et al., 2007) and far-field noise (Wasala et al., 2015; Geyer et al., 2016). In the past decade, the use of advanced turbulence modeling approaches within a computational fluid dynamics (CFD) framework, such as large-eddy simulations (LES) have become more popular. LES offers higher fidelity but also increases computational cost. There are several ways to represent rotating blades in CFD. These can be broadly classified based on whether the

blade surface is resolved or not. The class of blade-resolved CFD methods use a very fine mesh that closely follows the geometry of the blade and ensures a no-slip boundary condition at the surface of the blade. This mesh is then rotated over a stationary background mesh using one of several techniques like overset grids (Duan and Wang, 2020), sliding mesh (Steijl and Barakos, 2008; Aneesh et al., 2016), immersed boundary method (Stanly et al., 2020; Delorme et al., 2018; Müller et al., 2017; Mark and van Wachem, 2008), etc. It is computationally expensive to perform a complex multirotor simulation. Hence, the second classification of methods, where the blade is modelled using source terms, is preferred in cases where the local effects near the blade are of less importance compared to the flow effects caused by the tip vortices (Stanly, 2020).

Here, the rotor is modelled using a source term in the momentum equation using a class of methods called actuator methods, which avoids the need to resolve the surface of the blade, thereby saving a lot of computational effort. They are computationally efficient methods for representing lifting surfaces as a result of employing a forcing term in the momentum equation, as opposed to fully resolving them using densely spaced computational grid points. This saving in computational effort is done at the cost of reduced fidelity of representation of the lifting surface, but has been successful in predicting the far-field wake behind wind turbines (Sørensen et al., 2015). The broad subdivision of the actuator methods include actuator disc method (Lignarolo et al., 2016; Howland et al., 2016; Rocchio et al., 2018; Navarro Diaz et al., 2019; Micallef et al., 2020; de Jong Helvig et al., 2021), actuator line model (ALM)

Email address: ronithstanly@yahoo.com (Ronith Stanly)

¹In this work, the term *rotor* is used in the most general context where it refers to any rotating part (as opposed to a stationary part, say for instance, the *stator* in a gas turbine engine); i.e., both turbines and propellers are collectively referred to as *rotors* in this work.

55 and actuator surface method (ASM). The actuator disc method¹¹²
56 (Mikkelsen, 2003; Troldborg et al., 2015a; Ghaisas et al.,¹¹³
57 2020, 2018; Storey et al., 2015) represents the rotor as a disc¹¹⁴
58 consisting of radially varying, azimuthally averaged forces in¹¹⁵
59 the plane of the rotor. But this method has the drawback of¹¹⁶
60 shedding a vortex sheet instead of distinct tip vortices (Nathan¹¹⁷
61 et al., 2017; Nathan, 2018).¹¹⁸

62
63 The ALM was introduced by Sørensen and Shen (2002) as an¹²⁰
64 alternative to the actuator disc model (Sørensen and Myken,¹²¹
65 1992) and consists of representing the rotor as a rotating line¹²²
66 of radially varying forces, having one line for each blade.¹²³
67 At each instance of time, the velocity and local angle of¹²⁴
68 attack at each point on each line are extracted from the flow¹²⁵
69 solution (the accurate method for which is a hot research topic¹²⁶
70 (Churchfield et al., 2017)) and are used to look at airfoil tables¹²⁷
71 to find corresponding coefficients of lift and drag, which are¹²⁸
72 then used to compute the corresponding forces. The forces¹²⁹
73 are then projected onto the computational grid using some¹³⁰
74 projection function, which avoids the singular distribution of¹³¹
75 force (Churchfield et al., 2017). The most commonly used¹³²
76 method (Sørensen and Shen, 2002) is a three-dimensional¹³³
77 Gaussian function that is isotropic in width and fixed in¹³⁴
78 width along the blade span. Though this has been widely¹³⁵
79 successful in predicting far-field wakes, several issues have¹³⁶
80 been reported in literature and several correction measures¹³⁷
81 have been proposed. For example, Jha et al. (2014) clearly¹³⁸
82 showed the well-known problem of the method's inability to¹³⁹
83 correctly predict tip loads, for which tip and root corrections¹⁴⁰
84 were proposed (Shen et al., 2005). In another work, instead¹⁴¹
85 of using correction parameters, Shives and Crawford (2013)¹⁴²
86 used a three-dimensional Gaussian that is isotropically wide,¹⁴³
87 but that varies in width along the blade radius as a linear¹⁴⁴
88 function of local chord length based on the notion that since¹⁴⁵
89 the actuator line has discrete tips, it does not need additional¹⁴⁶
90 correction parameters. Jha et al. (2014) added to that work in¹⁴⁷
91 such a way that they did not scale the Gaussian width directly¹⁴⁸
92 with chord, but with an equivalent elliptical planform chord.¹⁴⁹
93 Martínez-Tossas et al. (2015) showed that the method had¹⁵⁰
94 trouble simultaneously matching experimentally measured¹⁵¹
95 power and thrust, which was attributed to the fact that the¹⁵²
96 isotropic Gaussian function projects the line force beyond¹⁵³
97 the tips. More recently, Churchfield et al. (2017) proposed a¹⁵⁴
98 variation of the isotropic Gaussian projection of Sørensen and¹⁵⁵
99 Shen (2002) that makes the projection function, and hence¹⁵⁶
100 the body force, look more like the force distribution on an¹⁵⁷
101 airfoil. Later, Jha and Schmitz (2018) proposed an actuator¹⁵⁸
102 curve embedding method which was aimed at overcoming the
103 fundamental problem of overlapping Gaussian distributions¹⁵⁹
104 between adjacent points, as seen in ALM and ASM.

105
106 Besides these mainstream advancements to ALM, some¹⁶¹
107 researchers incorporated a two-way coupling between the flow¹⁶²
108 solver and a structural solver to compute the deformation of¹⁶³
109 the actuator line and named it as the elastic actuator line (Meng¹⁶⁴
110 et al., 2018). This method is said to give better far-field wake¹⁶⁵
111 predictions and is also expected to give better predictions of¹⁶⁶

directivity when used for aeroacoustic predictions. Others have
used ALM along with Lattice Boltzmann flow solvers, like
Deiterding et al. (2018) and Rullaud et al. (2018) and with the
vortex particle-mesh method, like Caprace et al. (2019) and
Caprace (2020).

Besides the aforementioned types of ALM, there are ASMs
which are better at representing the rotor as compared to ALM.
ASM consists of representing a rotor not just as a single line,
but as a line consisting of smaller lines perpendicular to it at
different radial positions, representing chord lines of the rotor
blade sections. The chord-wise distribution of forces is meant
to give a better representation of the surface of the blade and
hence the near-wake. There are several implementations of
ASM (Dobrev et al., 2007; Shen et al., 2009; Sibuet Watters
and Masson, 2010; Yang and Sotiropoulos, 2018; Massie et al.,
2019); of these, the ones by Shen et al. (2009) and Yang and
Sotiropoulos (2018) are the ones that are based entirely on the
body force term, like the ALM. In the method by Shen et al.
(2009), the pressure distribution on the surface is represented
by body forces that are obtained using existing databases for
pressure and skin-friction distribution of airfoils and also the
ones calculated by Xfoil (Drela, 1989). The method by Yang
and Sotiropoulos (2018) is cheaper than the method by Shen
et al. (2009) since it uses chord-wise constant force (neglecting
chord-wise Coefficient-of-pressure-based variation of surface
forces).

Apart from these methods, very recently Martínez-Tossas
and Meneveau (2019) proposed a subgrid-scale velocity-
model-based ALM, called filtered ALM (F-ALM), which is
supposed to overcome the inefficiencies of the existing ALM
versions and enables LES/ALM on coarse grids (this is a
more theoretically consistent version of the model by Dağ and
Sørensen (2020); Dağ (2017)). In this work, we apply F-ALM
to a several-hundred-CPU-core LES of a wind turbine and
compare it with the baseline ALM.

We continue by describing the modelling framework in Section
2, then state the motivations for using F-ALM and give an
overview of its formulation in Section 3 and describe its
parallel implementation in Section 4. Following this, the newly
implemented parallel F-ALM is applied to simulate a National
Renewable Energy Laboratory (NREL) Phase VI wind turbine
in Section 5 and is compared to the baseline ALM. Finally, the
conclusions are summarised in Section 6.

2. Modelling Framework

The numerical methods implemented as part of this work are
added onto the in-house, high-order LES code, called **MIRA-
CLES** (which stands for multiblock-multiresolution immersed
boundary method reacting and compressible LES), which has
been well validated for complex aerodynamic problems over
the past couple of years (Delorme et al., 2017, 2018, 2020;
Stanly et al., 2020; Stanly, 2020; Hoffmann et al., 2020). A

167 brief overview of the numerical methods used in the code are 201
 168 shown in this section, whereas more elaborate details can be 202
 169 found in Stanly (2020) and Delorme et al. (2020). 203

170 2.1. Implicit Large-Eddy Simulation (LES) using MIRACLES 205

171 The filtered, compressible, Navier-Stokes equations for an
 172 ideal, calorically perfect gas are numerically integrated in the
 173 in-house flow solver called MIRACLES (Delorme et al., 2018),
 174 as shown in Eq.(1):

$$\frac{\partial \mathbf{U}}{\partial t} + \frac{\partial \mathbf{F}}{\partial x} + \frac{\partial \mathbf{G}}{\partial y} + \frac{\partial \mathbf{H}}{\partial z} = AD + \underbrace{\mathbf{f}}_{\text{Body Force}} \quad (1) \quad 206$$

175 where \mathbf{U} is the conservative variable vector and \mathbf{F} , \mathbf{G} and \mathbf{H} 207
 176 are flux vectors in the x , y and z directions, respectively. The 208
 177 term labeled AD on the right-hand side represents artificial 209
 178 dissipation (Delorme et al., 2018). The body-force source 210
 179 term, \mathbf{f} , is added to Eq.(1) if the ALM approach is chosen. The 211
 180 equations are solved on either structured Cartesian grids or 212
 181 body-fitted curvilinear grids. 213

182 Spatial discretization of the governing equations (Eq.(1)) for 214
 183 implicit LES is performed using 4th-order accurate Summation 215
 184 - By - Parts (SBP) (Strand, 1994) finite difference operators. An 216
 185 8th-order AD operator from Mattsson et al. (2004) is used for 217
 186 interior points, with a 4th-order boundary closure. Time inte- 218
 187 gration is performed via the 4th-order Runge-Kutta method. 219

189 2.1.1. Grid Stretching 221

190 MIRACLES code features both structured Cartesian and 222
 191 body-fitted curvilinear grid options. To enable grid refinement 223
 192 near a solid body or point of interest (say, for instance, the
 193 location of actuator lines), analytic grid stretching is utilized
 194 (Harlow and Welch, 1965; Delorme, 2013). LES computations
 195 are performed in computational space (ξ, η, ζ) , rather than 224
 196 physical space (x, y, z) . 225

197 The grid-stretching expression used is shown below: 226

$$N = 1 + (\exp(\chi) - 1) \left(\times \frac{\psi}{L} \right) \quad (2)$$

$$D = 1 + (\exp(-\chi) - 1) \left(\times \frac{\psi}{L} \right) \quad (3)$$

$$\gamma = \frac{1}{2\chi} \ln \left(\frac{N}{D} \right) \quad (4)$$

$$x = x_{min} + 1 + \frac{\sinh(\chi(\xi - \gamma))}{\sinh(\chi \times \gamma)} \left(\times \psi \right) \quad (5)$$

$$y = y_{min} + 1 + \frac{\sinh(\chi(\eta - \gamma))}{\sinh(\chi \times \gamma)} \left(\times \psi \right) \quad (6)$$

$$z = z_{min} + 1 + \frac{\sinh(\chi(\zeta - \gamma))}{\sinh(\chi \times \gamma)} \left(\times \psi \right) \quad (7) \quad 227$$

199 where χ controls the strength of clustering, ψ controls the loca- 228
 200 tion of stretching, L is the length of the domain in the stretching 230

direction, and x_{min} , y_{min} and z_{min} are the minimum values of
 the domain along the x , y and z directions. The values of the
 derivatives in the computational space are then computed using
 the chain rule (only the conversion from x space to ξ space is
 presented):

$$\frac{\partial}{\partial x} = \frac{\partial}{\partial \xi} \cdot \frac{\partial \xi}{\partial x} \quad (8)$$

$$\frac{\partial^2}{\partial x^2} = \frac{\partial^2}{\partial \xi^2} \left(\frac{\partial \xi}{\partial x} \right)^2 + \frac{\partial}{\partial \xi} \frac{\partial^2 \xi}{\partial x^2} \quad (9)$$

2.2. Actuator Line Modelling (ALM) of Rotors

In this work, the turbine and tower (which will be described
 in more detail in Section 2.3) are represented using actuator
 lines. Hence, instead of having a very fine grid that closely
 follows the geometry of the blades and tower, a coarser grid is
 used, onto which the rotor and tower are projected as forcing
 terms through the governing equation. As illustrated in Figure
 1, since we are using an isotropic, Gaussian function to spread
 the force onto the grid, the actuator lines project cylindrical
 blobs onto the grid. And when these actuator lines rotate, they
 shed helical tip vortices, which indicate flows having rotors.

2.2.1. Calculation of Forcing Terms

The steps involved in the calculation of the source terms are
 shown in Algorithm 1. To calculate the force terms, first, the
 flow velocity is extracted along the span of the rotor blade
 (Churchfield et al., 2017; Forsting and Troldborg, 2020) and the
 local station-wise velocity is computed as (Troldborg, 2009):

$$V_{rel} = \sqrt{V_z^2 + (\Omega r - V_\theta)^2} \quad (10)$$

where Ω is the angular velocity, V_z is the axial velocity and V_θ
 is the tangential velocity.

And the flow angle between V_{rel} and the rotor plane is:

$$\phi = \tan^{-1} \left(\frac{V_z}{\Omega r - V_\theta} \right) \quad (11)$$

From the above, the local angle of attack is given as:

$$\alpha = \phi - \gamma; \quad \gamma = \text{Sum of the local twist angle and twist of the blade} \quad (12)$$

From the local velocity and local angle of attack, the lift and
 drag per unit span are computed as:

$$\mathbf{f}_{2D} = (L, D) = \frac{1}{2} \rho V_{rel}^2 c(C_L \mathbf{e}_L, C_D \mathbf{e}_D) \quad (13)$$

where:

$$C_L = C_L(\alpha, Re) \text{ and } C_D = C_D(\alpha, Re) \quad (14)$$

and \mathbf{e}_L and \mathbf{e}_D are unit vectors in the direction of lift and drag.
 C_L and C_D are obtained from airfoil tables. Aerodynamic forces
 are distributed smoothly over several grid points to avoid sin-
 gular behaviour. Recently, several new methods were proposed

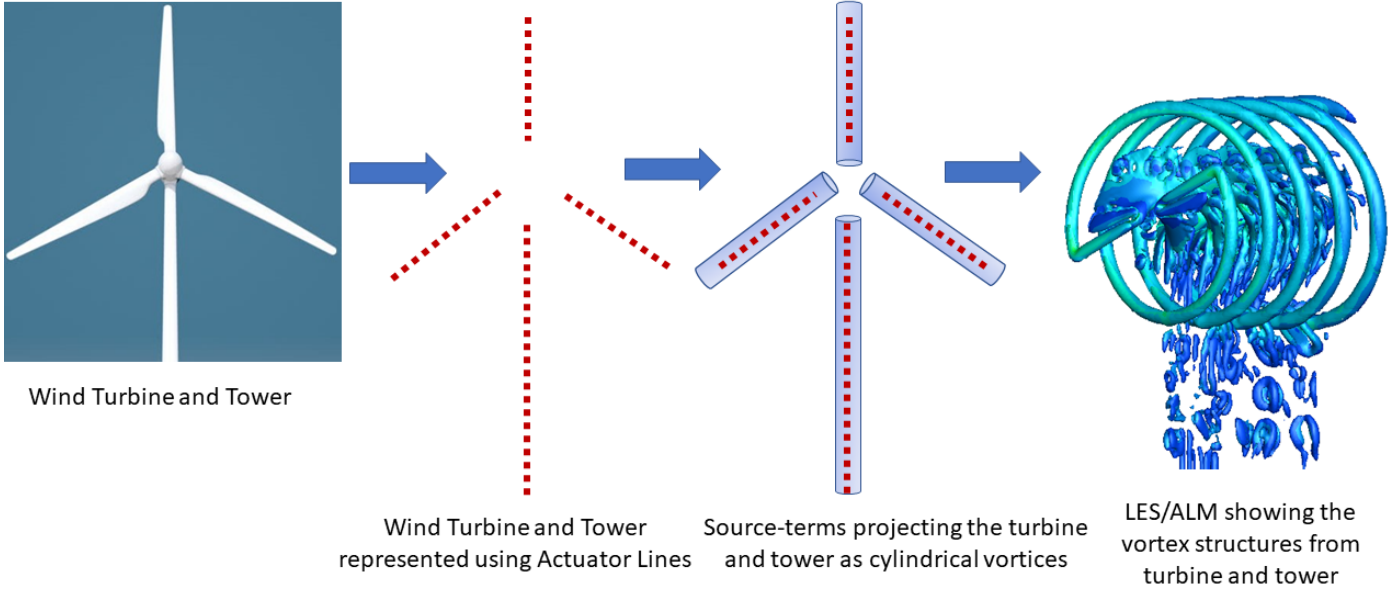


Figure 1: Representation of a wind turbine using actuator lines (Stanly, 2020).

Algorithm 1: Actuator Line Model (ALM)

Result: Compute source terms using ALM

```

1 while  $t < t_{end}$  do
2    $t = t + dt$ ;
3   for  $i \leftarrow 1$  to  $n\_blades$  do
4     Rotate blade to the new position;
5     for  $j \leftarrow 1$  to  $n\_radial\_sections$  do
6       Sample local in-flow velocity:
7          $V_{rel} = \sqrt{V_z^2 + (\Omega r - V_\theta)^2}$  (For a turbine);
8       Compute local angle of attack:
9          $\phi = \tan^{-1}\left(\frac{V_z}{\Omega r - V_\theta}\right)$  (For a turbine);
10      Look-up tables to find  $C_L, C_D$ :
11        $C_L = C_L(\alpha, Re)$  and  $C_D = C_D(\alpha, Re)$ ;
12      Compute lift and drag forces:
13        $\mathbf{f}_{2D} = (L, D) = \frac{1}{2}\rho V_{rel}^2 c(C_L \mathbf{e}_L, C_D \mathbf{e}_D)$ ;
14      Distribute forces onto LES grid: See
15        $F_x, F_y, F_z$  in Stanly (2020);
16     end
17   end
18 end
  
```

231 to do this. The first and the most common one is a three-
 232 dimensional Gaussian regularization kernel (η_ϵ):

$$\eta_\epsilon(d) = \frac{1}{\epsilon^3 \pi^{\frac{3}{2}}} \exp\left[-\frac{d^2}{\epsilon}\right] \quad (15)$$

233 where, $d = |\mathbf{x} - s\mathbf{e}_i|$ is the distance be-
 234 tween the grid point and the i^{th} actuator point; s is the coordi-
 235 nate of each station along the actuator line; \mathbf{e}_i is the unit vector;
 236 and ϵ is the spreading radius that adjusts the concentra-
 237 tion of regularized load.

238 Hence, the regularized load per unit volume is given as:
 239

$$\mathbf{f}_\epsilon(\mathbf{x}) = \sum_{i=1}^{N_{blades}} \left(\int_0^R \mathbf{f}_{2D}(s) \eta_\epsilon(|\mathbf{x} - s\mathbf{e}_i|) ds \right) \quad (16)$$

240 More subtleties about computing and projecting the source
 241 terms onto the CFD grid and how they vary between a turbine
 242 and a propeller can be found in Stanly (2020).

243 2.3. ALM for Turbine Towers

244 In order to include the presence of towers in the simulation at
 245 a reduced cost, actuator lines are used. This is, however, not
 246 exactly the same as having a tower represented using a fine
 247 body-fitted grid and having a no-slip boundary condition. The
 248 most prominent difference is the reduced magnitude of the
 249 stagnation pressure in front of the tower when ALM is used
 250 (Churchfield et al., 2015; Santoni et al., 2017; Kleusberg et al.,
 251 2017b). However, it is still capable of initiating the breakdown
 252 of the tip vortices.

253 A constant value is used for the coefficient of drag; in order to
 254 mimic the fluctuating forces from a cylinder experiencing von
 255

256 Karman vortex shedding, a fluctuating lift coefficient is used,³⁰³
 257 following the method used by Sarlak et al. (2015), as shown³⁰⁴
 258 below:

$$C_D = 1.2 \quad (17)^{307}$$

$$C_L = A \sin(2\pi ft) + B \quad (18)^{309}$$

259 where $f = 0.2U_\infty/D_{cyl}$ is the shedding frequency, D_{cyl} is the
 260 local diameter of the tower, $A = 0.3$ is the root mean square
 261 of lift coefficient at $Re \approx 10^5$ and B is a random parameter
 262 ($\sigma_B \approx \pm 0.25C_L$) added to the lift harmonic in order to resolve
 263 the unsteady nature of lift.
 264

265 3. Filtered ALM for Coarse-grid ALM

266 Although ALM allows us to have grids that are coarser than
 267 body-fitted grids, it is still computationally expensive when
 268 multiple rotors (such as in quadcopters or farms of wind tur-
 269 bines, for instance) need to be simulated. In actuator methods,
 270 a grid spacing (Δ) of $\Delta \approx \epsilon/2.8$ (where ϵ is the spreading radius
 271 onto which the source term is projected) or higher is preferred
 272 in order to smoothly distribute the forcing term onto more than
 273 two grid points, so as to avoid oscillations. Hence, while main-
 274 taining this constraint, a smaller ϵ (similar to the optimal value
 275 of $\epsilon = 0.25 \cdot c$ (Martínez-Tossas et al., 2017), where c is the lo-
 276 cal chord length) would mean many more grid points than for a
 277 bigger value of ϵ . Hence, it is desirable to go for a coarser-than-
 278 optimal value of the spreading function, ϵ , and hence a coarser
 279 grid.

280 3.1. Problems with Coarse-grid ALM

281 However, prior works (Stevens et al., 2018) have shown that
 282 even though a coarser spreading radius (i.e., a value for ϵ/c that
 283 is higher than 0.25, while still maintaining $\epsilon/\Delta \approx 2.8$) results in
 284 good predictions of downstream flow in terms of wakes in wind
 285 farms, the blade torque and power generation were too high,
 286 sometimes even exceeding the Betz limit (Martínez-Tossas and
 287 Meneveau, 2019).³¹⁰

288
 289 The reason is that, as shown in Figure 2, a wider spreading³¹²
 290 radius results in thicker, weaker tip vortices, which induces³¹³
 291 lower velocities, hence changing the effective angle of attack³¹⁴
 292 in the neighbouring blade sections and overpredicting torque³¹⁵
 293 and power. This is especially pronounced at the blade tip or³¹⁶
 294 regions in the blade where the lift coefficient or chord varies³¹⁷
 295 significantly (Martínez-Tossas and Meneveau, 2019).³¹⁸

296 3.2. Filtered-ALM (F-ALM)

297 To fix the overprediction of lift while using ALM on coarse
 298 grids, several tip corrections can be used (Jha et al., 2014; Shen
 299 et al., 2005; Zhong et al., 2019; Forsting. et al., 2019, 2020).³¹⁹
 300 But former ones were mostly based on empirical corrections³²⁰
 301 or fits, which may or may not work well depending on the³²¹
 302 blade. However, recently Martínez-Tossas and Meneveau³²²

(2019) added on to the work of Dağ (2017) and Dağ and
 Sørensen (2020) to come up with a well-derived subgrid-scale
 model, F-ALM, which prevents the overprediction of lift on
 coarse grids. The cyan-coloured text in Algorithm 2 shows the
 additional steps that need to be computed while using F-ALM
 as compared to ALM (which was shown in Algorithm 1).

Algorithm 2: Filtered - Actuator Line Model

Result: Compute source terms using F-ALM

```

1 while  $t < t_{end}$  do
2    $t = t + dt$ ;
3   for  $i \leftarrow 1$  to  $n\_blades$  do
4     Rotate blade to the new position;
5     for  $j \leftarrow 1$  to  $n\_radial\_sections$  do
6       Compute correction to downwash using
          sampled inflow velocity from  $(t - 1)$ :
           $u_y^{n*}(z_i; \epsilon_i) =$ 
           $-\frac{1}{U_\infty(z_i)} \int_{-\infty}^{\infty} \frac{dG^{n-1}(z')}{dz'} \frac{1}{4\pi(z_i - z')} \left( \left( 1 - e^{-(z_i - z')^2 / \epsilon_i^2} \right) dz' \right);$ 
7       Add velocity correction to sampled inflow
          velocity:  $\hat{\mathbf{u}}(\mathbf{x}_i) =$ 
           $\underbrace{\tilde{\mathbf{u}}(\mathbf{x}_i)}_{\text{Sampled}} + \left[ \underbrace{u_y(z_i; \epsilon^{opt})}_{\Delta u_y(\text{Model})} - u_y(z_i; \epsilon^{LES}) \right] \mathbf{j}$ ;
8       Use corrected inflow velocity to compute
          angle of attack:  $\phi = \tan^{-1} \left( \frac{V_z}{\Omega r - V_\theta} \right)$ 
9       Look-up tables to find  $C_L, C_D$ :
           $C_L = C_L(\alpha, Re)$  and  $C_D = C_D(\alpha, Re)$ ;
10      Compute lift and drag forces:
           $\mathbf{f}_{2D} = (L, D) = \frac{1}{2} \rho V_{rel}^2 c (C_L \mathbf{e}_L, C_D \mathbf{e}_D)$ ;
11      Distribute forces onto LES grid: See
           $F_x, F_y, F_z$  in Stanly (2020);
12    end
13  end
14 end
```

Following Martínez-Tossas and Meneveau (2019), in baseline
 ALM, we sample the fluid velocity, $\tilde{\mathbf{u}}(\mathbf{x}_i)$, at the i th actuator
 point, $\mathbf{x}_i = (x_i, y_i, z_i)$; this velocity is used to evaluate the lo-
 cal ALM force from tabulated lift and drag coefficients. For an
 infinite-span wing, the bound vorticity from the application of
 the ALM forces does not affect the sampled velocity. However,
 for a finite wing, the local velocity is affected by the induced
 velocity, $u_y(z_i; \epsilon^{LES})$. Hence, an approximation to the unper-
 turbed incoming velocity, $\mathbf{U}_\infty(\mathbf{x}_i)$, is given by:

$$\mathbf{U}_\infty(\mathbf{x}_i) = \underbrace{\tilde{\mathbf{u}}(\mathbf{x}_i)}_{\text{Sampled}} - \underbrace{u_y(z_i; \epsilon^{LES})}_{\text{Induced}} \mathbf{j} \quad (19)$$

where \mathbf{i} , \mathbf{k} and \mathbf{j} are unit vectors in the directions of $\mathbf{U}_\infty(\mathbf{x}_i)$, the
 blade span and the direction perpendicular to both (in the lift
 direction), respectively.

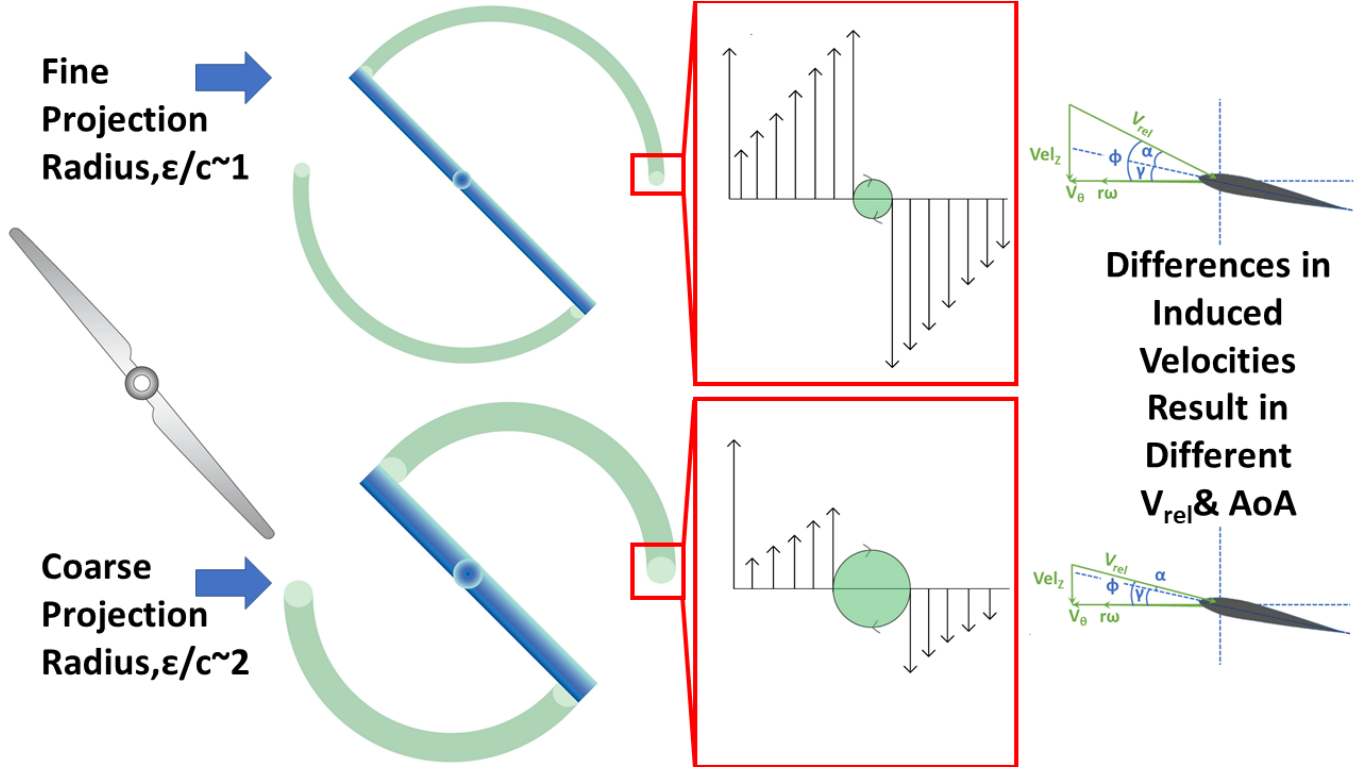


Figure 2: A coarse spreading radius (images on the lower part) resulting in wider (less concentrated) tip vortices, inducing weaker induced velocities and hence predicting the wrong angle of attack in the neighbouring actuator points, which will result in overprediction of lift. The vertical lines in the inset show the strength of induced velocities caused by the tip vortex.

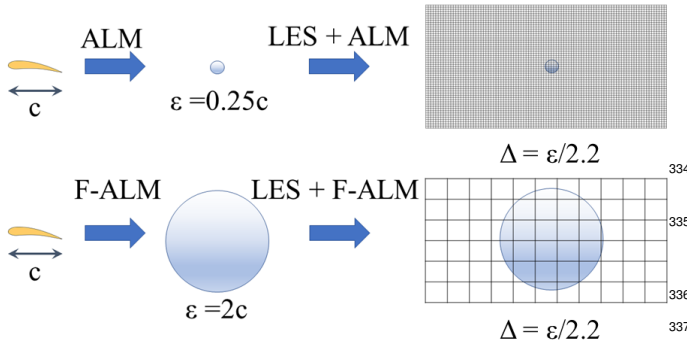


Figure 3: Grids and spreading radii used for ALM and F-ALM. Here, an $\epsilon/\Delta = 2.2$ is shown, but usually 2.8 or higher is preferred for a smooth distribution of the forcing term.

$$\hat{\mathbf{u}}(\mathbf{x}_i) = \underbrace{\tilde{\mathbf{u}}(\mathbf{x}_i)}_{\text{Sampled}} + \left[u_y(z_i; \epsilon^{opt}) - u_y(z_i; \epsilon^{LES}) \right] \mathbf{j} \quad (20)$$

where $\mathbf{U}_\infty(\mathbf{x}_i) = \underbrace{\tilde{\mathbf{u}}(\mathbf{x}_i)}_{\text{Sampled}} - \underbrace{u_y(z_i; \epsilon^{LES})}_{\text{Induced}} \mathbf{j}$, as shown in Eq.(19).

Thus, the difference $\Delta u_y = u_y(z_i; \epsilon^{opt}) - u_y(z_i; \epsilon^{LES})$ can be considered as the subfilter velocity model to be added to the LES-sampled velocity. The corrected velocity, $\hat{\mathbf{u}}(\mathbf{x}_i)$ (its magnitude and, importantly, its direction with modified angle of attack), can then be used in the determination of lift and drag coefficients as well as the direction of the applied ALM forces. The lift is applied perpendicular to $\hat{\mathbf{u}}(\mathbf{x}_i)$, the corrected inflow velocity at each radial section, whereas the drag force is parallel (Martínez-Tossas and Meneveau, 2019).

The velocity correction, Δu_y , can be obtained from the velocity perturbations (u_y) evaluated at the two (LES and optimal) ϵ values by implementing a numerical solution to the following equation:

$$u_y(z_i; \epsilon_k) = - \int_{-\infty}^{\infty} \frac{1}{U_\infty(z_i)} \frac{dG(z_j)}{dz_j} \frac{1}{4\pi(z_i - z_j)} \left(1 - e^{-(z_i - z_j)^2 / \epsilon_i^2} \right) dz_j \quad (21)$$

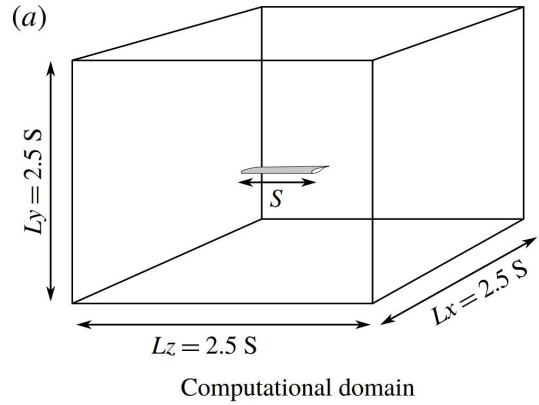


Figure 4: Translating wing test case from Martínez-Tossas and Meneveau (2019).

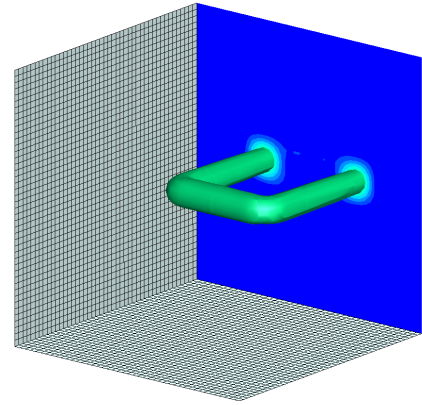


Figure 5: Vorticity magnitude of the static wing simulated using the current implementation in MIRACLES.

of our calculation with the ones of Martínez-Tossas and Meneveau (2019) are likely due to the fact that our work uses implicit LES while still employing an LES grid constructed using the criterion they followed ($\epsilon/dx = 2.8$) for their explicit LES simulation — instead of using a finer grid. However, for the NREL Phase VI case studied in subsequent sections, a finer grid is used after a careful grid sensitivity study. Nevertheless, Figure 6 shows that the current implementation of F-ALM captures the trend and the peak magnitudes sufficiently well, hence inferring the correctness of implementation of F-ALM.

4.3. Parallel Implementation

The main challenge with parallelizing F-ALM is the fact that the iterative solution at each actuator point along each line, within each time step, depends on the values at all other points on the same line through the integral and derivative in Eq.21. For other newer ALM methods (Jha and Schmitz, 2018; Dağ and Sørensen, 2020; Dağ, 2017), there are similar issues where the influence of neighbouring actuator points should be considered, and hence the solutions mentioned below can be applied to those methods too.

where u_y is the velocity perturbation evaluated at the current actuator point (i) using the k^{th} ϵ value, where k can be the LES value or the optimal value of the spreading function. $U_\infty(z_i)$ is the corrected inflow velocity at the current actuator point (i) from the previous time step; $G(z_j) = \frac{1}{2}c(z_j)U_\infty^2(z_j)c_L(z_j)$ is evaluated at all the other actuator points (j) on the same line along which the integration is to be performed. For a more detailed and complete description of the numerical integration of this equation, interested readers are encouraged to refer to Section 5 in the work by Martínez-Tossas and Meneveau (2019).

Thus, owing to this correction procedure, F-ALM allows us to have a spreading radius (and hence LES grid) that is coarser than the optimal value ($\epsilon^{opt} = 0.25 \cdot c$) without any overprediction of lift; this is schematically shown in Figure 3. It should, however, be noted that F-ALM does not change the shape of the tip vortex (i.e., in the blob projected onto the LES grid) to make it similar to the optimal case; it just corrects the induced velocity "felt" by the actuator points so that in the subsequent time steps, a more accurate angle of attack will be computed at these points, thereby resulting in a remedy for the overprediction of lift and hence power and torque.

4. Numerical Implementation

4.1. Serial Implementation

The procedure for implementing the subgrid-scale velocity correction in the actuator line model mentioned in Section 5 of Martínez-Tossas and Meneveau (2019) (also detailed in Stanly (2020)) is followed in this work.

4.2. Validation Using Translating Wing

The serial version of the F-ALM is validated using the translating wing case from Martínez-Tossas and Meneveau (2019), as shown in Figures 4, 5 and 6, using the parameters given in Table 1. It was applied to the test case using the same grid and spreading function (or filter or kernel size) specifications as used by Martínez-Tossas and Meneveau (2019).

Figure 5 shows the vorticity magnitude of the static wing simulated using the current implementation of F-ALM in MIRACLES, and Figure 6 shows the spanwise variation of normalized downwash (i.e., induced velocity perpendicular to the inflow) predicted by ALM and F-ALM on the same grid ($n_x = n_y = n_z = 44$) and LES filter/kernel size ($\epsilon^{LES}/c = 2$), using 200 actuator points. It can be seen in Figure 6 that, just as seen in the work of Martínez-Tossas and Meneveau (2019), the current implementation of F-ALM is able to predict a stronger downwash than the baseline ALM, hence validating the correctness of implementation. This is due to the fact that the F-ALM is able to mimic the effect of the stronger tip vortices on the same grid (but only at the actuator points) due to the subgrid velocity model, as mentioned in Section 3.2. Slight variations

Parameters	Expression	Value
Chord	c	0.32 m
Span Length	$S = 12.5 \times c$	4 m
LES filter/kernel size	$\epsilon^{LES} = 2 \times c$	0.64 m
Optimal filter/kernel size	$\epsilon^{OPT} = 0.25 \times c$	0.08 m
Grid Spacing	$dx = dy = dz = \frac{\epsilon^{LES}}{2.8}$	0.2285 m
Actuator Points		200
Domain Dimensions	$L_x = L_y = L_z = 2.5 \times S$	10 m
Airfoil Profile		NACA 64A17
Angle of Attack	α	6°
Coefficient of Lift	C_L	See Figure 11 and Table 4
Coefficient of Drag	C_D	0.000
Inflow Velocity	U_∞	1 m/s
Reynolds Number	Re	25000

Table 1: Values of parameters used to simulate the translating wing case and the expressions (from Martínez-Tossas and Meneveau (2019)) used to compute the dimensional quantities

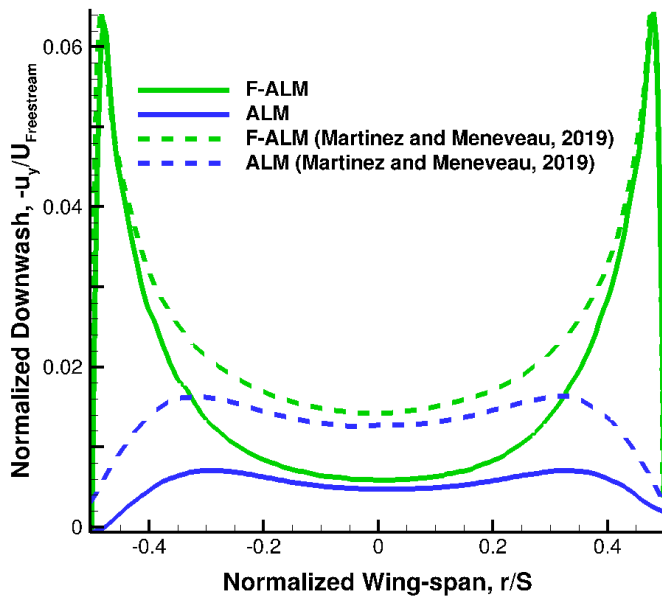


Figure 6: Spanwise variation of downwash simulated using ALM (green) and F-ALM (blue) using the current implementation (solid lines) in MIRACLES as compared to the one from Martínez-Tossas and Meneveau (2019) (dashed lines). The ability of F-ALM to predict the increased downwash, especially near the tips (as observed in Martínez-Tossas and Meneveau (2019)), ensures correctness of implementation. The variations between the current implementation and the reference results could be due to the inherent differences between the numerical schemes in the two codes; regardless of that, the current implementation correctly predicts the increased downwash at the tips.

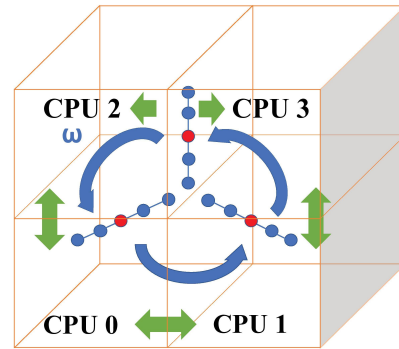


Figure 7: Three rotating blades split across four CPUs showing the complexity of data transfer with increasing CPUs.

A schematic representation is shown using actuator line representation of a three-bladed rotor split across four CPUs in Figure 7. Here, the solution at any actuator point on each actuator line (say, the red point) depends on all the other actuator points on the same line (the blue points). Hence, MPI messages (represented using green arrows) need to be sent between processors. However, since the local CPU ID of each actuator point keeps changing with time, due to the rotation of the actuator line, it is not feasible to send point-to-point MPI messages using `MPI_SEND` and `MPI_RECV` commands.

To handle this, the method mentioned in Algorithm 3 is followed. Here, at each time step, all CPUs belonging to a different blade are assigned to a new communicator, resulting in as many new communicators as there are blades (apart from the existing global communicator, `COMM_WORLD`). This is schematically shown in Figure 8, assuming three blades being divided into three new communicators, namely `COMM_1`, `COMM_2` and `COMM_3`, within the global communicator, `COMM_WORLD`. Then, within each new communicator, `MPI_GATHER` is performed to

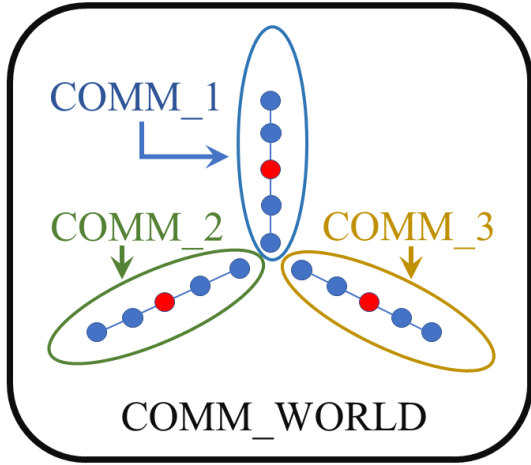


Figure 8: Schematic showing the global communicator encompassing three new communicators, one for each actuator line/blade.

gather the required data from across the concerned actuator line into the CPU 0 of that communicator. Then, the F-ALM computation that depends on the neighbouring points are performed in that CPU. Following this, MPI_BCAST is used to broadcast the velocity corrections at each actuator point onto their respective CPUs and the remaining calculations are done. For a more detailed description of the parallel implementation and its testing, interested readers are referred to read Stanly (2020).

Algorithm 3: MPI algorithm for communicating between actuator points

```

1 while  $t < t_{end}$  do
2    $t = t + dt$ ;
3   for  $i \leftarrow 1$  to  $n.blades$  do
4     Rotate the blade to the new position;
5     MPI_COMM_SPLIT splits COMM_WORLD into
      separate communicators for each blade;
6     Within each new communicator MPI_GATHER
      data from all points on each line into its CPU 0;
7     Perform F-ALM (or any new ALM) calculations
      that depend on neighbouring points in CPU 0
      of each new communicator;
8     MPI_BCAST the velocity correction from CPU 0
      to all the CPUs in that communicator;
9     Continue with Step 6 of F-ALM as in Algorithm
      2 from the respective CPUs (these are localised
      computations);
10  end
11 end

```

5. NREL Phase VI Wind Turbine

Since the advantage of F-ALM compared to ALM shows up mainly on the blade loads, the NREL Phase VI experiment is

simulated in this section, since it has experimental blade measurements to compare to. The case is simulated using both ALM and F-ALM employing the same coarser-than-optimal spreading radius of $\epsilon/c = 0.5$, on the same LES grid of 15 million points constructed using an average $\epsilon/\Delta = 3.6$ (as shown in Table 3), and their differences are studied here. However, this test case does not have measured experimental wake velocity profiles, so wake comparisons are made with other simulation results from literature. The test conditions of the test sequence H of the two-bladed, single-turbine, NREL Phase VI experiment (Churchfield et al., 2017; Jonkman, 2003) are simulated in this section. The test conditions are shown in Table 2. The blade twist is obtained from Table 6.9 on page 96 of Jonkman (2003). It should be noted that an additional pitch of 1.51° is given to this twist distribution at all actuator points, to obtain the 3° twist at the tip, as used in the experiment for this test sequence.

5.1. Computational Setup

The domain used for simulating the NREL Phase VI case is shown in Figure 9. The rotor plane is located at the origin (with its center equidistant from all boundaries) while the tower is placed $1.4m \equiv 0.28R$ behind the rotor plane and is represented using an actuator line having a cylinder of diameter, $D_{cyl} = 0.5m \equiv 0.1R$ (to be used in Eq.(18)). The structured, stretched (stretching toward the origin) grid created using the parameters shown in Table 3 is shown in Figure 10. Stretching is limited in the streamwise (Z) direction so as to have almost equally finely spaced grid points in order to capture the wake vortex dynamics, whereas there is increased grid stretching at the rotor plane (X - Y) in order to increase the clustering of points in the rotor disc region. Care was taken to ensure that the stretching along the vertical axis (Y) was smooth enough to ensure the tower was represented smoothly while also allowing good clustering of points near the rotor disc. The solution was computed on 729 CPUs. For both ALM and F-ALM simulations, the same coarser-than-optimal spreading radius of $\epsilon/c = 0.5$, on the same LES grid of 15 million points constructed using an average $\epsilon/\Delta = 3.6$ (as shown in Table 3), is employed.

Airfoil tables, to be used in the calculation of actuator line source terms, are taken from Table 6.8 on page 95 of Jonkman (2003) and as elaborated on pages 163-172 in Jonkman (2003). It is also shown in Figure 11. The initial cylindrical portion of the blade is modelled using a constant $C_L = 0.0$ and $C_D = 0.3$, thereafter a single C_D curve is used for all the stations, as shown in Figure 11. The different coefficient of lift curves are used depending on the location of the actuator point as shown in Table 4.

Uniform, non-turbulent inflow is used as an inflow boundary condition, and outflow boundary condition is used on the opposite side. Since the wind tunnel where this experiment was conducted is much larger than the domain used in this simulation, a slip boundary condition is imposed on the walls in order to eliminate the presence of no-slip walls at locations different

Characteristic	Symbol	Value
Rotor Radius	R	5.029 m
Mean Chord	C_{mean}	0.5475m \equiv 0.1095R
Airfoils		S809
Blade Pitch, in Addition to the Twist		1.51°
Number of Blades per Turbine	N_b	2
Number of Turbines and Towers		1
Tip-Speed Ratio	TSR	5.35
Inflow Velocity	U_∞	7 m/s
Rotations per Minute	RPM	71.9 RPM
Tip Velocity	U_{ref}	37.86 m/s
Tip Mach Number	M_{Tip}	0.1
Tip Reynolds Number	Re_{Tip}	1×10^6

Table 2: Test Conditions of the NREL Phase VI Experiment (Sequence H)

Characteristic	Symbol	Value
Size of Domain	$L_x \times L_y \times L_z$	$4.8R \times 4.8R \times 4.8R$
Grid Points per CPU	$n_{xCPU} \times n_{yCPU} \times n_{zCPU}$	$25 \times 25 \times 33$
Total Number of CPUs	$n_{CPU,x} \times n_{CPU,y} \times n_{CPU,z}$	$9 \times 9 \times 9 = 729$
Total Grid Points	$n_x \times n_y \times n_z$	$225 \times 225 \times 297 = 15 \times 10^6$
Strength of Grid Stretching	$\chi_x \times \chi_y \times \chi_z$	$3 \times 3 \times 1$
Average Grid Size in the Rotor Plane	$dx \times dy \times dz$	$0.0152R \times 0.0152R \times 0.0155R$
Average Grid Size of the Coarsest Cells	$dx \times dy \times dz$	$0.0353R \times 0.0353R \times 0.0174R$
Number of Actuator Points per Line		50
Spreading Radius	ϵ	$0.5 \times C_{mean}$
Average Rotor Plane Grid Size in terms of ϵ	Δ	$\epsilon/3.6$

Table 3: Grid parameters used for the NREL Phase VI case (same values are used for both ALM and F-ALM)

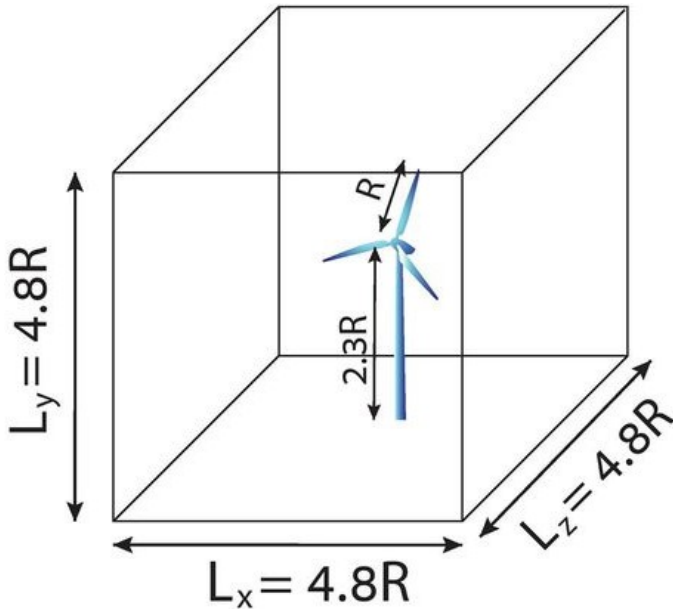


Figure 9: Domain used for simulating the NREL Phase VI test case. The rotor plane is at the origin (i.e., center of the domain). Please note that the three-bladed turbine shown in this figure is only for the purpose of illustration; the actual turbine simulated in this work is a two-bladed turbine.

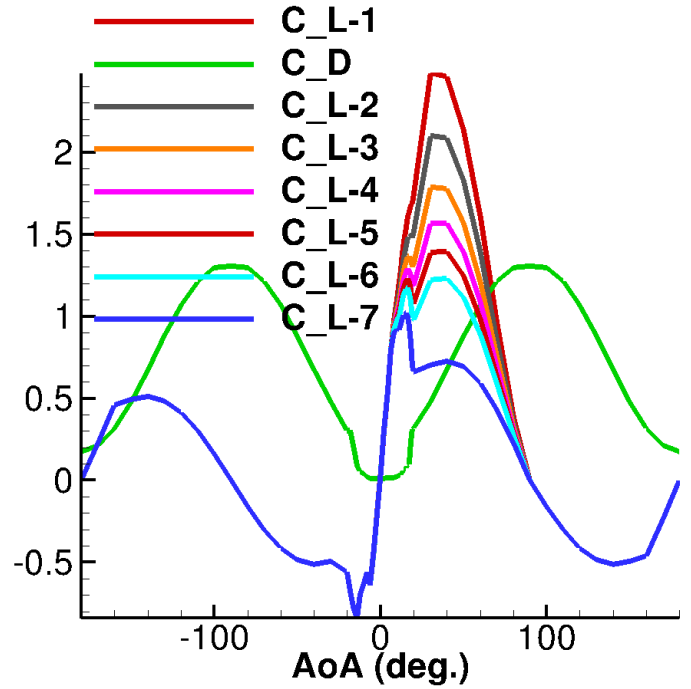


Figure 11: The airfoil tables used for the NREL Phase VI case taken from Table 6.8 on page 95 of Jonkman (2003) and as elaborated on pages 163-172 in Jonkman (2003). The different coefficient-of-lift curves are used depending on the location of the actuator point as shown in Table 4.

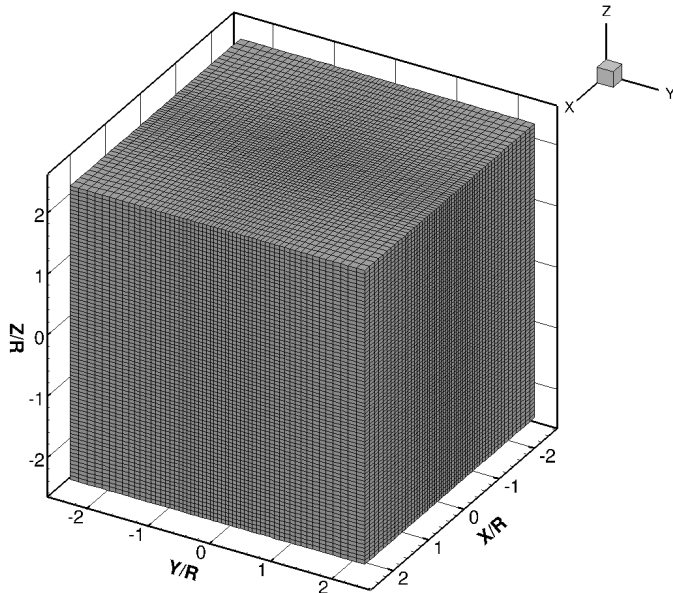


Figure 10: Grid used for the NREL Phase VI test case. Every fourth grid point is shown here. Notice increased grid stretching along the \$X\$ and \$Y\$ axes.

Coefficient-of-Lift Curve	Location of Actuator Points
$C_L - 1$	< 12.9% Span
$C_L - 2$	< 18.9% Span
$C_L - 3$	< 24.2% Span
$C_L - 4$	< 29.8% Span
$C_L - 5$	< 35.4% Span
$C_L - 6$	< 41.0% Span
$C_L - 7$	$\geq 41.0\%$ Span

Table 4: Usage of the C_L curves shown in Figure 11 based on the spanwise location of actuator points

513 from those in the experiment. The simulation is run for 3 non-562
514 dimensional time units (NTUs)². The initial transients disap-
515 pear after the initial 1 NTU, but the solution for one more NTU⁵⁶³
516 is computed before averaging is done in the third NTU. This is⁵⁶⁴
517 done to ensure that the flow has reached a statistically steady⁵⁶⁵
518 state. Blade loads are also averaged during the third NTU. A⁵⁶⁶
519 time step of $0.001 \times \frac{R}{U_{ref}} \equiv 0.001 \times t_{ref} = 1.32 \times 10^{-4} s$ is used⁵⁶⁷
520 for this simulation.

521 5.2. Model Parameter Sensitivity

522 To ensure that the solution is separate of the LES grid used in⁵⁷⁴
523 this study, an independent grid study was performed based on⁵⁷⁵
524 the Richardson extrapolation method (ASME, 2008). Solution⁵⁷⁶
525 of LES/ALM on three grids were computed, as shown in Table⁵⁷⁷
526 5. The rule of thumb of having $\epsilon/\Delta > 2$ was maintained⁵⁷⁸
527 for the "fine" and "medium" grids; while that could not be⁵⁷⁹
528 maintained for the "coarse" grid (as we maintained a constant⁵⁸⁰
529 $\epsilon/c = 0.5$ for the spreading radius for all three cases), its⁵⁸¹
530 solution still did not have any spurious fluctuations and the⁵⁸²
531 source term was smoothly distributed onto the LES grid. As⁵⁸³
532 mentioned earlier in Section 5.1, the simulation was run for 3⁵⁸⁴
533 NTUs and time-averaging was performed in the third NTU. It⁵⁸⁵
534 should be noted that tests were conducted where averaging was⁵⁸⁶
535 performed for more NTUs, but it did not show any difference in⁵⁸⁷
536 the averaged results, presumably because of the non-turbulent⁵⁸⁸
537 inflow condition and because the initial transients already⁵⁸⁹
538 left the domain after the first NTU. The time-averaged power⁵⁹⁰
539 predicted using the three LES grids, shown in Table 5, was⁵⁹¹
540 used to compute the grid convergence index (GCI) using a⁵⁹²
541 fixed point iteration of Eq.3 found in ASME (2008) to obtain⁵⁹³
542 a GCI of 6% for the "fine" grid, which was then used in the⁵⁹⁴
543 LES/ALM and LES/F-ALM computations mentioned in the⁵⁹⁵
544 remainder of this work.

545
546 The number of actuator points along all actuator lines was al-⁵⁹⁸
547 ways kept as 50, based on suggestions from other works in liter-⁵⁹⁹
548 ature (Sarлак et al., 2015; Ravensbergen et al., 2020; Martínez,⁶⁰⁰
549 2017) and based on our own trials, which showed its indepen-⁶⁰¹
550 dence beyond that value. For the size of the spreading radius⁶⁰²
551 based on the chord length (ϵ/c), even though the optimal value⁶⁰³
552 is 0.25 (Martínez-Tossas et al., 2017), since we wanted to com-⁶⁰⁴
553 pare the influence of F-ALM on the solution (which can be⁶⁰⁵
554 pronounced, as compared to ALM, if the spreading radius and⁶⁰⁶
555 hence its associated LES grid is coarser), a slightly higher value⁶⁰⁷
556 of $\epsilon/c = 0.5$ is used in this work. The time step used in this⁶⁰⁸
557 work is about one order of magnitude smaller than what other⁶⁰⁹
558 users typically use for wind turbine simulations, and is good⁶¹⁰
559 enough to take care of the compressible nature of the code.⁶¹¹
560 Smaller time steps were examined, but did not show any no-⁶¹²
561 ticeable difference in key parameters.

²1 NTU is the time taken for a particle to travel from the inlet to the outlet⁶¹⁶
of the domain (Sarлак et al., 2015)

5.3. Results

5.3.1. Flow field

568 The instantaneous flow structures produced by the two LES
569 simulations, namely LES/ALM as well as LES/F-ALM, are
570 shown in Figure 12 using the iso-surface of Q-Criterion (with
571 a value of $Q = 35m^2s^{-2}$) coloured by vorticity magnitude.
572 Both these simulations show the dominant tip vortices in a
573 physically correct manner and are similar to what is found in
literature (Churchfield et al., 2017; Ravensbergen et al., 2020;
Lynch et al., 2014). There is some vorticity that is shed from
the inboard parts of the blades, which is more dominant at the
spanwise stations that had increased twist. Even though the
actuator-line-modelled tower presents some disturbance to the
tip vortices, the domain used here is not long enough to observe
the tip vortex breakdown far downstream. As seen in literature
(Churchfield et al., 2015; Ravensbergen et al., 2020), the
disruption caused by the actuator-line-modelled tower to the tip
vortices is less than what could have resulted in the presence
of towers represented using no-slip surfaces on body-fitted
grids. This could be explained by the lower stagnation pressure
(caused by the lower resistance to the flow) induced in front of
the tower by the actuator-line-modelled tower, as compared to
a tower represented using no-slip surfaces (Churchfield et al.,
2015). And as expected, Figure 12 shows no difference in
the flow field between LES/ALM and LES/F-ALM, since the
change made to the source term is prominent only at the tip
and root of the blade and that change cannot be "seen" in the
flow field unless the grid is fine enough for that. However, the
main aim of achieving a better prediction of blade loads as
compared to ALM on the same coarser-than-optimal mesh is
achieved by using F-ALM, as will be explained in Section 5.3.2.

An axial slice of Figure 12 is taken through a plane enclosing
the tower (see YZ plane in Figure 9), and instantaneous and
time-averaged plots of the wake (streamwise velocity (w)
normalized by inflow velocity, $w_{inf} = U_{\infty}$) are shown in
Figures 13 and 14. The blockage caused to the flow by
the rotor plane can be clearly noticed from the low-velocity
region ahead of the rotor plane accompanied by the region
of increased velocities beyond the rotor plane. Since there
are no experimental wake velocity profiles available for this
experiment, we quantitatively compare the wake with other
simulations (Ravensbergen et al., 2020), as shown in Figure
15, where the time-averaged streamwise velocity is extracted
from and plotted along a vertical line $2R$ downstream of the
turbine (i.e., at $Z = -2R$ along a line that stretched from
 $Y = -2.4R$ to $Y = +2.4R$). The trend of the velocity profile
agrees well with the reference simulation by having a strong
velocity deficit behind the rotor plane (due to the presence of
the turbines that extract energy from the incoming flow); it also
shows the fluctuations in the velocity behind the tower. There
are disagreements in the magnitude of the wake deficit profile,
including behind the tower, nacelle and lower part of the rotor
(due to interaction with the tower in the simulation) and also
between 50% and the tips. It is because of the fact that the sim-
ulation (Ravensbergen et al., 2020) to which we are comparing

Grid	Points	Edge Length	ϵ/Δ	Power (kW)	Refinement Ratio	GCI (%)
1 Coarse	3 466 008	0.0276 R	1.85	6.675 kW	–	–
2 Medium	6 993 756	0.0219 R	2.33	6.557 kW	1.26	–
3 Fine	13 002 444	0.0152 R	3.60	6.778 kW	1.44	6%

Table 5: Grid independence study

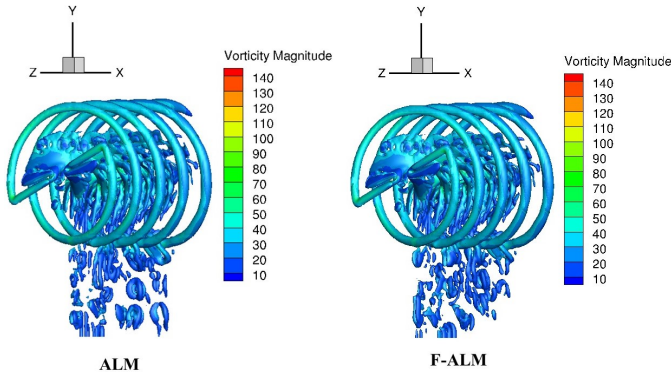


Figure 12: Instantaneous flow structures of the NREL Phase VI wind turbine are shown using the iso-surface of the Q-Criterion with a value of $Q = 35m^2s^{-2}$ coloured by vorticity magnitude. LES/ALM is on the left and LES/F-ALM on the right, showing no noticeable difference in flow structures between the two.

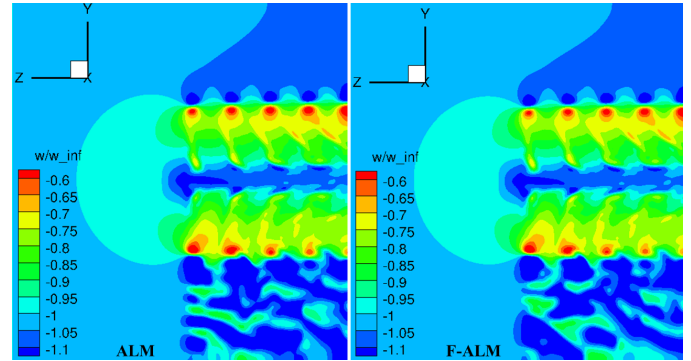


Figure 13: Instantaneous wake (streamwise velocity (w) normalized by inflow velocity, $w_{inf} = U_{\infty}$) of the NREL Phase VI wind turbine is shown on the YZ plane, which contains the tower. LES/ALM is on the left and LES/F-ALM is on the right, showing no noticeable difference in flow structures between the two. The flow is from left to right in both images.

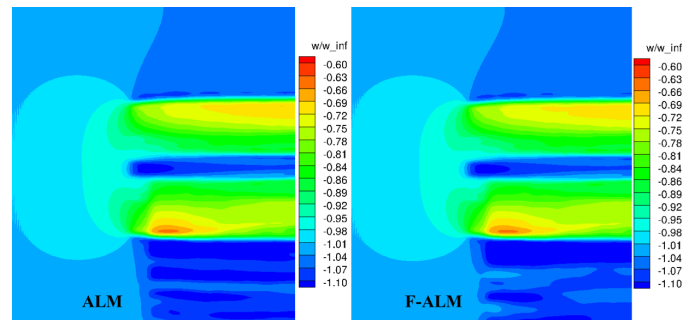


Figure 14: Time-averaged wake (streamwise velocity (w) normalized by inflow velocity, $w_{inf} = U_{\infty}$) of the NREL Phase VI wind turbine is shown on the YZ plane, which contains the tower. LES/ALM is on the left and LES/F-ALM is on the right, showing no noticeable difference in flow structures between the two. The flow is from left to right in both images.

our profile is not exactly the same as this simulation, since it had the tower and nacelle included in the simulation using a body-fitted grid and a weakly enforced no-slip boundary condition (whereas we did not model the nacelle and modelled the tower using an actuator line, as mentioned earlier). The better representation of the tower and nacelle resulted in an increased velocity deficit in their simulation, and also resulted in an increased interaction with the tip vortices from the lower part of the rotor plane (Churchfield et al., 2015; Santoni et al., 2017). As seen in other works in literature (Santoni et al., 2017), the disagreement in the wake deficit between 50% and the top tip of the rotor is also caused by the lack of a nacelle, which is most pronounced nearest to the rotor plane (as in the case shown here, where we investigate at 1D downstream) and reduces as we move further downstream (about 6D or more). However, since there are no further simulation or experimental wake measurements for this case, we could not compare that. A more detailed study of wind turbine cases with wake measurements, like the NTNU Blind Tests (Fabio et al., 2012), are currently being investigated and will be published in due course. However, the present simulation captures the expected trend quite well.

5.3.2. Blade Loads

Next, in order to study the influence of F-ALM and to see how it differs from ALM for the same LES grid and spreading radius, we compare the time-averaged measurements at the blades (or actuator lines). As discussed in Section 3, since F-ALM corrects the induced velocity at the blades, we compare

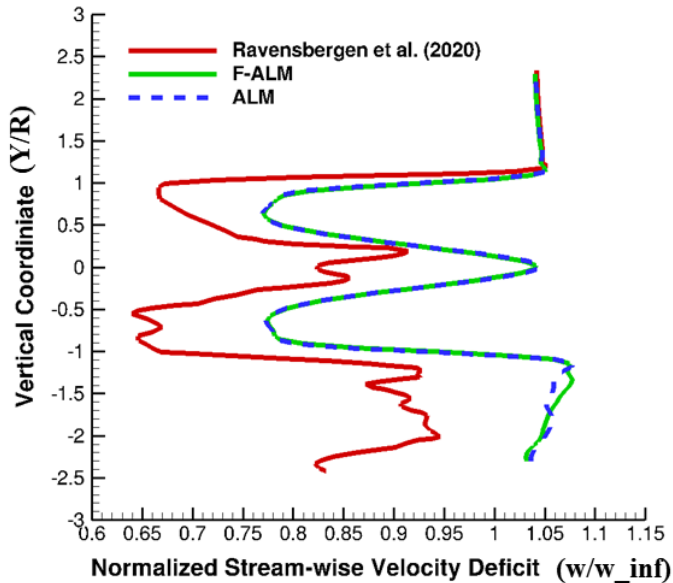


Figure 15: Time-averaged wake velocity deficit (streamwise velocity (w) normalized by inflow velocity, $w_{inf} = U_{\infty}$) of the NREL Phase VI wind turbine along a vertical line ($Y = -2.4R$ to $+2.4R$) $2R$ downstream of the turbine (at $Z = -2R$).

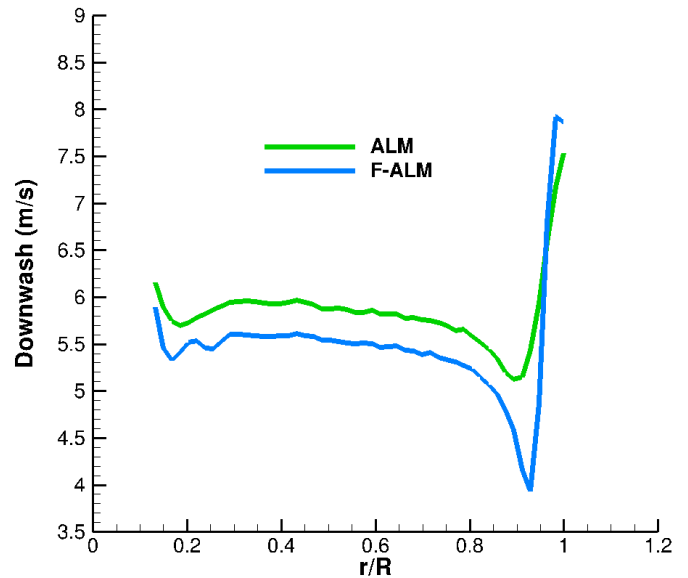


Figure 16: Time-averaged induced velocity measured at the actuator points along the blade span.

647 the time-averaged (and also averaged between the two blades)
 648 induced velocity at the blades for LES/ALM, as well as LES/F-
 649 ALM, as shown in Figure 16. It can be seen that F-ALM
 650 predicts a stronger downwash (i.e., induced velocity perpendicular
 651 to the inflow) than ALM, and hence represents the effect of
 652 a stronger and a more concentrated tip vortex, than ALM on the
 653 same grid. This effect is more pronounced near the tip and root
 654 of the blade, as expected, and shows the significance of F-ALM.
 655

656 To see how this change in induced velocity affects the blade
 657 loads and hence the power prediction, we compare the time-
 658 averaged chord-wise tangential force coefficient along the
 659 blade, as shown in Figure 17. As expected, F-ALM corrects the
 660 force that ALM overpredicted, and this is more significantly
 661 observed at the blade root and tip. The reason why both
 662 simulations gave a massive overshoot in the predicted force
 663 near the root is probably due to the three-dimensional rotational
 664 effects (Banga, 2017; Branlard, 2017; Lehmkühl et al., 2013)
 665 that are present in the rotor blades, which are not captured well
 666 by actuator simulations since two-dimensional airfoil tables are
 667 used in computing the source terms.
 668

669 Next, the power produced is compared in Table 6; ALM over-
 670 predicts power by 12.96%, whereas F-ALM gives only a slight
 671 overprediction of 1%. This clearly shows the advantage of using
 672 F-ALM over ALM.

Experiment	ALM	F-ALM
6.0 kW	6.778 kW	6.06 kW

Table 6: Power produced by NREL Phase VI turbine

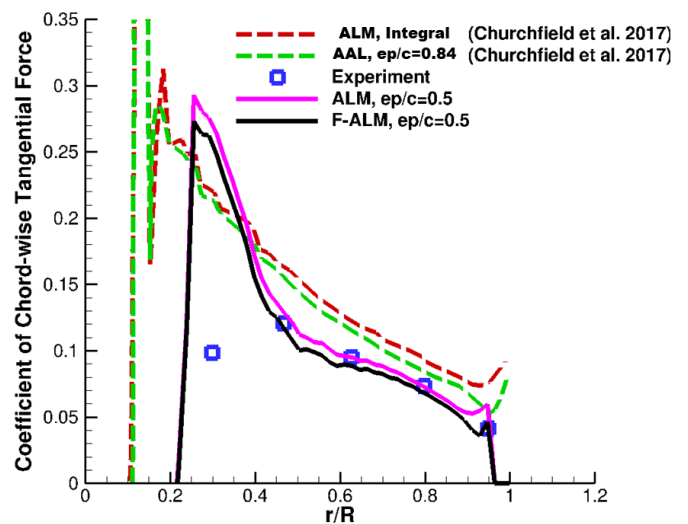


Figure 17: The time-averaged coefficients of the chord-wise tangential force obtained at the actuator points along the blade span with the current ALM and F-ALM simulations are shown in magenta and black solid lines, respectively. The experimental values (Jonkman, 2003) are shown as blue squares. In addition, for comparison, simulation results from Churchfield et al. (2017) are shown with dotted lines: the red dotted line corresponds to ALM with a constant uniform Gaussian projection function and integral velocity sampling, and the green dotted line corresponds to advanced ALM with chord-thickness Gaussian and integral sampling.

5.3.3. Computational Time

The average time per time step for computing LES/ALM and LES/F-ALM was checked on 8 CPU cores, as shown in Table 7. It can be seen that F-ALM computation took just an additional 1% of time to compute each time step.

ALM	F-ALM
3.0098 s	3.039 s

Table 7: Average time per time step for ALM and F-ALM computations

6. Conclusions and Future Work

In this work, we implemented the recently developed, F-ALM into a high-order, in-house LES code and used it in a several-hundred-CPU simulation of a wind turbine. The solution of F-ALM was then compared to that of the baseline ALM in terms of instantaneous and time-averaged flow fields and blade loads. The effect of the sub-grid model was observed in terms of the induced velocity at the blade, with F-ALM predicting stronger induced velocities mainly at the root and tip as expected, and then in the blade loads. It was observed that F-ALM overpredicted power only by 1%, whereas ALM overpredicted it by 12.96%. However, as expected, the flow field produced by F-ALM did not show any noticeable difference from the flow field produced by ALM. Any deviations in the wake results observed as compared to other simulations in literature were mainly due to the lack of a nacelle and body-fitted-grid-simulated tower.

Future work includes modelling the nacelle, probably using an actuator disc, and including the tower using the immersed boundary method. More elaborate work involving F-ALM and its application to several other wind turbine cases of increasing complexity is underway. Enhancing the capability of the in-house code to have turbulent inflow (Forsting et al., 2019) is also under consideration. Since F-ALM allows coarser LES grids, it is more suitable for LES simulations having explicit subgrid-scale models (Ciri et al., 2018), rather than the currently used implicit LES; hence, that will also be explored in future works.

7. Acknowledgments

Prof. David Wood from the University of Calgary, Canada is acknowledged for his suggestions and notes about blade element momentum theory, which helped in the implementation of ALM. Prof. Stefano Markidis from KTH Royal Institute of Technology, Stockholm, Sweden and Prof. David Greenblatt from Technion - Israel Institute of Technology, Haifa, Israel are acknowledged for their suggestions, which helped increase the quality of this work. Maria Jarrous is thanked for helping with some of the illustrations used in this work. This work has received funding from the European Union's Horizon 2020 research and innovation program under grant agreement

No.815278 on behalf of the NEMMO Project.

This work was authored in part by the National Renewable Energy Laboratory, operated by Alliance for Sustainable Energy, LLC, for the U.S. Department of Energy (DOE) under Contract No. DE-AC36-08GO28308. Funding provided by U.S. Department of Energy Office of Energy Efficiency and Renewable Energy Wind Energy Technologies Office. The views expressed in the article do not necessarily represent the views of the DOE or the U.S. Government. The U.S. Government retains and the publisher, by accepting the article for publication, acknowledges that the U.S. Government retains a nonexclusive, paid-up, irrevocable, worldwide license to publish or reproduce the published form of this work, or allow others to do so, for U.S. Government purposes.

References

- Aneesh, D.S., Stanly, R., Sagaram, S.B., Suneesh, S.S., 2016. Numerical analysis of magnus wind turbine, in: 2016 7th International Conference on Mechanical and Aerospace Engineering (ICMAE), pp. 191–195. doi:10.1109/ICMAE.2016.7549533.
- ASME, 2008. Procedure for Estimation and Reporting of Uncertainty Due to Discretization in CFD Applications. Journal of Fluids Engineering 130. URL: <https://doi.org/10.1115/1.2960953>, doi:10.1115/1.2960953. 078001.
- Bangga, G.S.T.A., 2017. Three-Dimensional Flow in the Root Region of Wind Turbine Rotors. Ph.D. thesis. University of Stuttgart. URL: <http://www.uni-kassel.de/upress/online/OpenAccess/978-3-7376-0536-6.OpenAccess.pdf>.
- Benard, P., Viré, A., Moureau, V., Lartigue, G., Beaudet, L., Deglaire, P., Bricteux, L., 2018. Large-eddy simulation of wind turbine wakes including geometrical effects. Computers & Fluids 173, 133 – 139. URL: <http://www.sciencedirect.com/science/article/pii/S0045793018301154>, doi:<https://doi.org/10.1016/j.compfluid.2018.03.015>.
- Bouras, I., Ma, L., Ingham, D., Pourkashanian, M., 2018. An improved k – turbulence model for the simulations of the wind turbine wakes in a neutral atmospheric boundary layer flow. Journal of Wind Engineering and Industrial Aerodynamics 179, 358 – 368. URL: <http://www.sciencedirect.com/science/article/pii/S0167610518301296>, doi:<https://doi.org/10.1016/j.jweia.2018.06.013>.
- Branlard, E., 2017. Wind Turbine Aerodynamics and Vorticity-Based Methods. URL: <https://www.springer.com/gp/book/9783319551630>, doi:10.1007/978-3-319-55164-7.
- Caprace, D.G., 2020. Modeling of lifting-dragging devices for large eddy simulation of space-developing wakes : application to wings, rotors and formation flight. Ph.D. thesis. UC Louvain. URL: <http://hdl.handle.net/2078.1/239381>.
- Caprace, D.G., Buffin, S., Duponcheel, M., Chatelain, P., Winckelmans, G., 2017. Large Eddy Simulation of Advancing Rotor for Near to Far Wake Assessment. URL: <http://hdl.handle.net/20.500.11881/3812>.
- Caprace, D.G., Chatelain, P., Winckelmans, G., 2019. Lifting line with various modifications: Theory and application to an elliptical wing. AIAA Journal 57, 17–28. URL: <https://doi.org/10.2514/1.J057487>, doi:10.2514/1.J057487.
- Caprace, D.G., Chatelain, P., Winckelmans, G., 2020. Wakes of rotorcraft in advancing flight: A large-eddy simulation study. Physics of Fluids 32, 087107. URL: <https://doi.org/10.1063/5.0015162>, doi:10.1063/5.0015162.
- Caprace, D.G., Winckelmans, G., Chatelain, P., 2021. Assessment of the Vortex Particle-Mesh Method for Efficient LES of Hovering Rotors and their Wakes. URL: <https://arc.aiaa.org/doi/abs/10.2514/6.2021-0738>, doi:10.2514/6.2021-0738.
- Churchfield, M.J., Lee, S., Schmitz, S., Wang, Z., 2015. Modeling Wind Turbine Tower and Nacelle Effects within an Actuator Line Model. URL: <https://arc.aiaa.org/doi/>

- abs/10.2514/6.2015-0214, doi:10.2514/6.2015-0214, arXiv:https://arc.aiaa.org/doi/pdf/10.2514/6.2015-0214
- Churchfield, M.J., Schreck, S.J., Martínez, L.A., Meneveau, C., Spalart, P.R., 2017. An advanced actuator line method for wind energy applications and beyond. 35th Wind Energy Symposium, AIAA SciTech Forum 2017-1998. URL: https://www.nrel.gov/docs/fy17osti/67611.pdf, doi:10.2514/6.2017-1998.
- Ciri, U., Petrolo, G., Salvetti, M.V., Leonardi, S., 2020. Large-eddy simulations of two in-line turbines in a wind tunnel with different inflow conditions. *Energy* 10, 821. URL: https://www.mdpi.com/1996-1073/10/6/821, doi:https://doi.org/10.3390/en10060821.
- Ciri, U., Salvetti, M.V., Carrasquillo, K., Santoni, C., Iungo, G.V., Leonardi, S., 2018. Effects of the subgrid-scale modeling in the large-eddy simulations of two in-line turbines, in: Grigoriadis, D.G., Geurts, B.J., Kuerten, H., Fröhlich, J., Armenio, V. (Eds.), *Direct and Large-Eddy Simulation X*, Springer International Publishing, Cham, pp. 109–115.
- Dağ, K., 2017. Combined pseudo-spectral / actuator line model for wind turbine applications. Ph.D. thesis.
- Dağ, K.O., Sørensen, J.N., 2020. A new tip correction for actuator line computations. *Wind Energy* 23, 148–160. URL: https://onlinelibrary.wiley.com/doi/abs/10.1002/we.2419, doi:10.1002/we.2419.
- Deiterding, R., Gkoudesnes, C., Cox, A., 2018. Application of lattice-boltzmann methods for large-eddy simulation of wind turbine rotor wake aerodynamics. 6th European Conference on Computational Mechanics (ECCM 6), June URL: http://www.eccm-ecfd2018.org/admin/files/fileabstract/a1978.pdf.
- Delorme, Y., 2013. High order Large Eddy Simulation of unpowered and powered Fontan hemodynamics in idealized and patient specific geometries. Ph.D. thesis. Purdue. URL: https://docs.lib.purdue.edu/dissertations/AAI3604761/.
- Delorme, Y., Stanly, R., Frankel, S.H., Greenblatt, D., 2020. Application of actuator line model for large eddy simulation of rotor noise control. *Aerospace Science and Technology*, 106405 URL: http://www.sciencedirect.com/science/article/pii/S1270963820310877, doi:https://doi.org/10.1016/j.ast.2020.106405.
- Delorme, Y.T., Frankel, S.H., Jain, R., Strawn, R., 2017. Performance Assessment of High-Order Large Eddy Simulation and Immersed Boundary Method for Rotorcraft Hover. URL: https://arc.aiaa.org/doi/abs/10.2514/6.2017-0539, doi:10.2514/6.2017-0539, arXiv:https://arc.aiaa.org/doi/pdf/10.2514/6.2017-0539.
- Delorme, Y.T., Frankel, S.H., Jain, R., Strawn, R., 2018. High-order large eddy simulation and immersed boundary method on dynamic meshes: Application to rotorcraft aerodynamics. *AIAA SciTech Forum* URL: https://arc.aiaa.org/doi/10.2514/6.2018-0599, doi:10.2514/6.2018-0599.
- Dobrev, I., Massouh, F., Rapin, M., 2007. Actuator surface hybrid model. *Journal of Physics: Conference Series* 75. URL: https://iopscience.iop.org/article/10.1088/1742-6596/75/1/012019, doi:10.1088/1742-6596/75/1/012019.
- Drela, M., 1989. Xfoil: An analysis and design system for low Reynolds number airfoils. *Low Reynolds Number Aerodynamics: Proceedings of the Conference Notre Dame, Indiana, USA, 5–7 June* URL: http://web.mit.edu/drela/Public/papers/xfoil_sv.pdf, doi:10.1007/978-3-642-84010-4_1.
- Duan, Z., Wang, Z.J., 2020. High-order overset flux reconstruction method for dynamic moving grids. *AIAA Journal* 0, 1–14. URL: https://doi.org/10.2514/1.J059185, doi:10.2514/1.J059185, arXiv:https://doi.org/10.2514/1.J059185.
- Dörenkämper, M., Witha, B., Steinfeld, G., Heinemann, D., Kühn, M., 2015. The impact of stable atmospheric boundary layers on wind-turbine wakes within offshore wind farms. *Journal of Wind Engineering and Industrial Aerodynamics* 144, 146–153. URL: http://www.sciencedirect.com/science/article/pii/S0167610514002694, doi:https://doi.org/10.1016/j.jweia.2014.12.011. selected papers from the 6th International Symposium on Computational Wind Engineering CWE 2014.
- Fabio, P., Pal, Egil, E., Lars, S., Per-Age, K., 2012. Invitation to the 2012 "blind test 2" workshop calculations for two wind turbines in line. URL: http://www.norcowe.no/doc/NORCOWE-NOWITECH%20joint%20workshop%202012%20-%20invite[2].pdf.
- Forsting, A.R.M., Pirrung, G.R., Ramos-García, N., 2019. A vortex-based tip/smearing correction for the actuator line. *Wind Energy Science* 4, 369–383. URL: https://wes.copernicus.org/articles/4/369/2019/, doi:10.5194/wes-4-369-2019.
- Forsting, A.R.M., Pirrung, G.R., Ramos-García, N., 2019. The wake of an actuator line with a vortex-based tip/smearing correction in uniform and turbulent inflow. *Journal of Physics: Conference Series* 1256, 012020. URL: https://doi.org/10.1088/1742-6596/1256/1/012020, doi:10.1088/1742-6596/1256/1/012020.
- Forsting, A.R.M., Pirrung, G.R., Ramos-García, N., 2020. Brief communication: A fast vortex-based smearing correction for the actuator line. *Wind Energy Science* 5, 349–353. URL: https://wes.copernicus.org/articles/5/349/2020/, doi:10.5194/wes-5-349-2020.
- Forsting, A.R.M., Troldborg, N., 2020. Generalised grid requirements minimizing the actuator line angle-of-attack error. *Journal of Physics: Conference Series* 1618, 052001. URL: https://doi.org/10.1088/1742-6596/1618/5/052001, doi:10.1088/1742-6596/1618/5/052001.
- Geyer, T.F., Wasala, S.H., Cater, J.E., Norris, S.E., Sarradj, E., 2016. Experimental Investigation of Leading Edge Hook Structures for Wind Turbine Noise Reduction. URL: https://arc.aiaa.org/doi/abs/10.2514/6.2016-2954, doi:10.2514/6.2016-2954.
- Ghaisas, N.S., Ghate, A.S., Lele, S.K., 2018. Large-eddy simulation study of multi-rotor wind turbines. *Journal of Physics: Conference Series* 1037, 072021. URL: https://doi.org/10.1088/1742-6596/1037/7/072021, doi:10.1088/1742-6596/1037/7/072021.
- Ghaisas, N.S., Ghate, A.S., Lele, S.K., 2020. Effect of tip spacing, thrust coefficient and turbine spacing in multi-rotor wind turbines and farms. *Wind Energy Science* 5, 51–72. URL: https://wes.copernicus.org/articles/5/51/2020/, doi:10.5194/wes-5-51-2020.
- Harlow, F.H., Welch, J.E., 1965. Numerical calculation of time-dependent viscous incompressible flow of fluid with free surface. *The Physics of Fluids* 8, 2182–2189. URL: https://aip.scitation.org/doi/abs/10.1063/1.1761178, doi:10.1063/1.1761178.
- Hoffmann, N., Delorme, Y.T., Frankel, S.H., 2020. High-Order Large Eddy Simulations of High-Speed Boundary Layer Transition. URL: https://arc.aiaa.org/doi/abs/10.2514/6.2020-0033, doi:10.2514/6.2020-0033, arXiv:https://arc.aiaa.org/doi/pdf/10.2514/6.2020-0033.
- Howland, M.F., Bossuyt, J., Martínez-Tossas, L.A., Meyers, J., Meneveau, C., 2016. Wake structure in actuator disk models of wind turbines in yaw under uniform inflow conditions. *Journal of Renewable and Sustainable Energy* 8, 043301. URL: https://doi.org/10.1063/1.4955091, doi:10.1063/1.4955091, arXiv:https://doi.org/10.1063/1.4955091.
- Ivanell, S., Sørensen, J.N., Henningson, D., 2007. Numerical computations of wind turbine wakes, in: Peinke, J., Schaumann, P., Barth, S. (Eds.), *Wind Energy*, Springer Berlin Heidelberg, Berlin, Heidelberg, pp. 259–263.
- Jha, P.K., Churchfield, M.J., Moriarty, P.J., Schmitz, S., 2014. Guidelines for volume force distributions within actuator line modeling of wind turbines on large-eddy simulation-type grids. *Journal of Solar Energy Engineering* 136. URL: http://solarenergyengineering.asmedigitalcollection.asme.org/article.aspx?articleid=1790335, doi:10.1115/1.4026252.
- Jha, P.K., Schmitz, S., 2018. Actuator curve embedding – an advanced actuator line model. *Journal of Fluid Mechanics* 834, R2. doi:10.1017/jfm.2017.793.
- de Jong Helvig, S., Vinnes, M.K., Segalini, A., Worth, N.A., Hearst, R.J., 2021. A comparison of lab-scale free rotating wind turbines and actuator disks. *Journal of Wind Engineering and Industrial Aerodynamics* 209, 104485. URL: http://www.sciencedirect.com/science/article/pii/S0167610520303950, doi:https://doi.org/10.1016/j.jweia.2020.104485.
- Jonkman, J., 2003. Modeling of the use wind turbine for refinement of fast.ad. NREL Technical Report URL: https://www.nrel.gov/docs/fy04osti/34755.pdf.
- Kleusberg, E., 2019. Wind-turbine wakes - Effects of yaw, shear and turbine interaction. Ph.D. thesis. KTH, Stability, Transition and Control. QC20190514.
- Kleusberg, E., Mikkelsen, R.F., Schlatter, P., Ivanell, S., Henningson, D.S., 2017a. High-order numerical simulations of wind turbine wakes. *Journal of Physics: Conference Series* 854, 012025. URL: https://doi.org/10.1088/1742-6596/854/1/012025, doi:10.1088/1742-6596/854/1/012025.
- Kleusberg, E., Mikkelsen, R.F., Schlatter, P., Ivanell, S., Henningson, D.S., 2017b. High-order numerical simulations of wind turbine wakes. *Journal of Physics: Conference Series* 854, 012025. URL: https://doi.org/10.1088/1742-6596/854/1/012025, doi:10.1088/1742-6596/854/1/012025.

- 926 D.S., 2017b. High-order numerical simulations of wind turbine wakes. *Journal of Physics: Conference Series* 854, 012025. URL: <https://doi.org/10.1088/1742-6596/854/1/012025>. doi:10.1088/1742-6596/854/1/012025.
- 927
928
929
930 Kleusberg, E., Sarmast, S., Schlatter, P., Ivanell, S., Henningson, D.S., 2016. Actuator line simulations of a joukowski and tjareborg rotor using spectral element and finite volume methods. *Journal of Physics: Conference Series* 753, 082011. URL: <https://doi.org/10.1088/1742-6596/753/8/082011>. doi:10.1088/1742-6596/753/8/082011.
- 931
932
933
934
935 Kleusberg, E., Schlatter, P., Henningson, D.S., 2020. Parametric dependencies of the yawed wind-turbine wake development. *Wind Energy* 23, 1367–1380. URL: <https://onlinelibrary.wiley.com/doi/abs/10.1002/we.2395>. doi:10.1002/we.2395.
- 936
937
938
939 Korobenko, A., Yan, J., Gohari, S., Sarkar, S., Bazilevs, Y., 2017. FSI simulation of two back-to-back wind turbines in atmospheric boundary layer flow. *Computers & Fluids* 158, 167 – 175. URL: <http://www.sciencedirect.com/science/article/pii/S0045793017301718>. doi:10.1016/j.compfluid.2017.05.010.
- 940
941
942
943
944 eddy and direct numerical simulations of oceanic and atmospheric flows. *Lehmkuhl, O., Rodríguez, I., Baez, A., Oliva, A., Pérez-Segarra, C., 2013. On the large-eddy simulations for the flow around a dynamic profiles using unstructured grids. Computers & Fluids* 84, 176 – 189. URL: <http://www.sciencedirect.com/science/article/pii/S0045793013002144>. doi:10.1016/j.compfluid.2013.06.002.
- 945
946
947
948
949
950
951 Lignarolo, L.E., Mehta, D., Stevens, R.J., Yilmaz, A.E., van Kuik, G., Andersen, S.J., Meneveau, C., Ferreira, C.J., Ragni, D., Meyers, J., van Bussel, G.J., Holierhoek, J., 2016. Validation of four LES and a vortex model against stereo-piv measurements in the near wake of an actuator disc and a wind turbine. *Renewable Energy* 94, 510 – 523. URL: <http://www.sciencedirect.com/science/article/pii/S0960148116302543>. doi:10.1016/j.renene.2016.03.070.
- 952
953
954
955
956
957
958
959 Lynch, C., Prosser, D., Smith, M., 2014. An efficient actuating blade model for unsteady rotating system wake simulations. *Computers & Fluids* 92, 138 – 150. URL: https://fun3d.larc.nasa.gov/papers/lynch_candf_2013.pdf. doi:10.1016/j.compfluid.2013.12.014.
- 960
961
962
963
964 Mark, A., van Wachem, B.G., 2008. Derivation and validation of a novel implicit second-order accurate immersed boundary method. *Journal of Computational Physics* 227, 6660 – 6680. URL: <https://www.sciencedirect.com/science/article/pii/S0021999108001770>. doi:10.1016/j.jcp.2008.03.031.
- 965
966
967
968
969 Martínez, L.A., 2017. Large Eddy Simulations and Theoretical Analysis of Wind Turbine Aerodynamics Using an Actuator Line Model. Ph.D. thesis. Johns Hopkins University. URL: <https://jscholarship.library.jhu.edu/handle/1774.2/44708>.
- 970
971
972
973 Martínez-Tossas, L.A., Churchfield, M.J., Leonardi, S., 2015. Large eddy simulations of the flow past wind turbines: actuator line and disk modeling. *Wind Energy* 18, 1047–1060. URL: <https://onlinelibrary.wiley.com/doi/abs/10.1002/we.1747>. doi:10.1002/we.1747.
- 974
975
976
977 Martínez-Tossas, L.A., Meneveau, C., 2019. Filtered lifting line theory and application to the actuator line model. *Journal of Fluid Mechanics* 863, 269–292. doi:10.1017/jfm.2018.994.
- 978
979
980 Martínez-Tossas, L.A., Churchfield, M.J., Meneveau, C., 2017. Optimal smoothing length scale for actuator line models of wind turbine blades based on gaussian body force distribution. *Wind Energy* 20, 1083–1096. URL: <https://onlinelibrary.wiley.com/doi/abs/10.1002/we.2081>. doi:10.1002/we.2081.
- 981
982
983
984
985 Massie, L., Ouro, P., Stoesser, T., Luo, Q., 2019. An actuator surface model to simulate vertical axis turbines. *Energies* 12, 4741. URL: <https://doi.org/10.3390/en12244741>. doi:10.3390/en12244741.
- 986
987
988
989 Mattsson, K., Svard, M., Nordstrom, J., 2004. Stable and accurate artificial dissipation. *Journal of Scientific Computing* 21, 57–79. URL: <https://link.springer.com/article/10.1023/B:JOMP.0000027955.75872.3f>. doi:10.1023/B:JOMP.0000027955.75872.3f.
- 990
991
992
993 Meng, H., Lien, F.S., Li, L., 2018. Elastic actuator line modelling for wake-induced fatigue analysis of horizontal axis wind turbine blade. *Renewable Energy* 116, 423 – 437. URL: <http://www.sciencedirect.com/science/article/pii/S0960148117308364>. doi:10.1016/j.renene.2017.08.074.
- 994
995
996 Micallef, D., Ferreira, C., Herráez, I., Höning, L., Yu, W., Capdevila, H., 2020. Assessment of actuator disc models in predicting radial flow and wake expansion. *Journal of Wind Engineering and Industrial Aerodynamics* 207, 104396. URL: <http://www.sciencedirect.com/science/article/pii/S0167610520303068>. doi:10.1016/j.jweia.2020.104396.
- Mikkelsen, R., 2003. Actuator Disc Methods Applied to Wind Turbines. Ph.D. thesis. Technical University of Denmark. URL: http://orbit.dtu.dk/fedora/objects/orbit:85749/datastreams/file_5452244/content.
- Mohamed, A.B., Bear, C., Bear, M., Korobenko, A., 2020. Performance analysis of two vertical-axis hydrokinetic turbines using variational multiscale method. *Computers & Fluids* 200, 104432. URL: <http://www.sciencedirect.com/science/article/pii/S0045793020300086>. doi:10.1016/j.compfluid.2020.104432.
- Müller, B., Krämer-Eis, S., Kummer, F., Oberlack, M., 2017. A high-order discontinuous galerkin method for compressible flows with immersed boundaries. *International Journal for Numerical Methods in Engineering* 110, 3–30. URL: <https://onlinelibrary.wiley.com/doi/abs/10.1002/nme.5343>. doi:10.1002/nme.5343.
- Nathan, J., 2018. Application of actuator surface concept in LES simulations of the near wake of wind turbines. Ph.D. thesis. École de Technologie Supérieure, Université du Québec. URL: <http://espace.etsmtl.ca/id/eprint/2088>.
- Nathan, J., Forsting, A.R.M., Trolldborg, N., Masson, C., 2017. Comparison of OpenFOAM and EllipSys3d actuator line methods with (NEW) MEXICO results. *Journal of Physics: Conference Series* 854, 012033. URL: <https://doi.org/10.1088/1742-6596/854/1/012033>. doi:10.1088/1742-6596/854/1/012033.
- Navarro Diaz, G.P., Saulo, A.C., Otero, A.D., 2019. Wind farm interference and terrain interaction simulation by means of an adaptive actuator disc. *Journal of Wind Engineering and Industrial Aerodynamics* 186, 58 – 67. URL: <http://www.sciencedirect.com/science/article/pii/S0167610518308237>. doi:10.1016/j.jweia.2018.12.018.
- Ouro, P., Stoesser, T., 2017. An immersed boundary-based large-eddy simulation approach to predict the performance of vertical axis tidal turbines. *Computers & Fluids* 152, 74 – 87. URL: <http://www.sciencedirect.com/science/article/pii/S0045793017301202>. doi:10.1016/j.compfluid.2017.04.003.
- Porté-Agel, F., Wu, Y.T., Lu, H., Conzemius, R.J., 2011. Large-eddy simulation of atmospheric boundary layer flow through wind turbines and wind farms. *Journal of Wind Engineering and Industrial Aerodynamics* 99, 154 – 168. URL: <http://www.sciencedirect.com/science/article/pii/S0167610511000134>. doi:10.1016/j.jweia.2011.01.011. the Fifth International Symposium on Computational Wind Engineering.
- Ravensbergen, M., Mohamed, A.B., Korobenko, A., 2020. The actuator line method for wind turbine modelling applied in a variational multiscale framework. *Computers & Fluids* 201, 104465. URL: <http://www.sciencedirect.com/science/article/pii/S0045793020300384>. doi:10.1016/j.compfluid.2020.104465.
- Richards, P., Norris, S., 2011. Appropriate boundary conditions for computational wind engineering models revisited. *Journal of Wind Engineering and Industrial Aerodynamics* 99, 257 – 266. URL: <http://www.sciencedirect.com/science/article/pii/S0167610510001418>. doi:10.1016/j.jweia.2010.12.008. the Fifth International Symposium on Computational Wind Engineering.
- Richards, P., Norris, S., 2015. Appropriate boundary conditions for a pressure driven boundary layer. *Journal of Wind Engineering and Industrial Aerodynamics* 142, 43 – 52. URL: <http://www.sciencedirect.com/science/article/pii/S016761051500063X>. doi:10.1016/j.jweia.2015.03.003.
- Richards, P.J., Norris, S.E., 2019. Appropriate boundary conditions for computational wind engineering: Still an issue after 25 years. *Journal of Wind Engineering and Industrial Aerodynamics* 190, 245 – 255. URL: <http://www.sciencedirect.com/science/article/pii/S0167610518306615>. doi:10.1016/j.jweia.2019.05.012.
- Rocchio, B., Ciri, U., Salvetti, M.V., Leonardi, S., 2020. Appraisal

- and calibration of the actuator line model for the prediction of turbulent separated wakes. *Wind Energy* 23, 1231–1248. URL: <https://doi.org/10.1002/we.2483>, doi:<https://doi.org/10.1002/we.2483>.
- Rocchio, B., Deluca, S., Salvetti, M., Zanforlin, S., 2018. Development of a bem-cfd tool for vertical axis wind turbines based on the actuator disk model. *Energy Procedia* 148, 1010 – 1017. URL: <http://www.sciencedirect.com/science/article/pii/S1876610218303515>, doi:<https://doi.org/10.1016/j.egypro.2018.08.060>. aTI 2018 73rd Conference of the Italian Thermal Machines Engineering Association
- Rullaud, S., Blondel, F., Cathelain, M., 2018. Actuator-line model in a lattice boltzmann framework for wind turbine simulations. *Journal of Physics: Conference Series* 1037. URL: <https://iopscience.iop.org/article/10.1088/1742-6596/1037/2/022023>, doi:<https://doi.org/10.1088/1742-6596/1037/2/022023>.
- Santoni, C., Carrasquillo, K., Arenas-Navarro, I., Leonardi, S., 2017. Effect of tower and nacelle on the flow past a wind turbine. *Wind Energy* 20, 1927–1939. URL: <https://onlinelibrary.wiley.com/doi/abs/10.1002/we.2130>, doi:<https://doi.org/10.1002/we.2130>.
- Sarлак, H., Meneveau, C., Sørensen, J., 2015. Role of subgrid-scale modeling in large eddy simulation of wind turbine wake interactions. *Renewable Energy* 77, 386 – 399. URL: <http://www.sciencedirect.com/science/article/pii/S0960148114008635>, doi:<https://doi.org/10.1016/j.j.renene.2014.12.036>.
- Sarmast, S., Dadfar, R., Mikkelsen, R.F., Schlatter, P., Ivanell, S., Sørensen, J., Henningson, D., 2014a. Mutual inductance instability of the tip vortices behind a wind turbine. *Journal of Fluid Mechanics* 755, 705–731. doi:[10.1017/jfm.2014.326](https://doi.org/10.1017/jfm.2014.326).
- Sarmast, S., Schlatter, P., Ivanell, S., Mikkelsen, R.F., Henningson, D.S., 2014b. Instability of the helical tip vortices behind a single wind turbine in: Hölling, M., Peinke, J., Ivanell, S. (Eds.), *Wind Energy - Impact of Turbulence*, Springer Berlin Heidelberg, Berlin, Heidelberg. pp. 165–174.
- Shen, W.Z., Sørensen, J.N., Mikkelsen, R., 2005. Tip loss correction for actuator/navier–stokes computations. *Journal of Solar Energy Engineering* 127, 1172–1174. URL: <http://solarenergyengineering.asmedigitalcollection.asme.org/article.aspx?articleid=1457272>, doi:[10.1115/1.1850488](https://doi.org/10.1115/1.1850488).
- Shen, W.Z., Zhang, J.H., Sørensen, J.N., 2009. The actuator surface model: A new navier–stokes based model for rotor computations. *Journal of Solar Energy Engineering* 131(1), 011002–011002–9. URL: <http://solarenergyengineering.asmedigitalcollection.asme.org/article.aspx?articleid=1474410>, doi:[10.1115/1.3027502](https://doi.org/10.1115/1.3027502).
- Shives, M., Crawford, C., 2013. Mesh and load distribution requirements for actuator line cfd simulations. *Wind Energy* 16, 1183–1196. URL: <https://onlinelibrary.wiley.com/doi/abs/10.1002/we.1546>, doi:<https://doi.org/10.1002/we.1546>.
- Sibuet Watters, C., Masson, C., 2010. Modeling of lifting-device aerodynamics using the actuator surface concept. *International Journal of Numerical Methods in Fluids* 62, 1264–1298. URL: <https://onlinelibrary.wiley.com/doi/abs/10.1002/flid.2064>, doi:[10.1002/flid.2064](https://doi.org/10.1002/flid.2064).
- Sørensen, J.N., Mikkelsen, R.F., Henningson, D.S., Ivanell, S., Sarmast, S., Andersen, S.J., 2015. Simulation of wind turbine wakes using the actuator line technique. *Philosophical Transactions of the Royal Society A: Mathematical, Physical and Engineering Sciences* 373, 20140071. URL: <https://royalsocietypublishing.org/doi/full/10.1098/rsta.2014.0071>, doi:[10.1098/rsta.2014.0071](https://doi.org/10.1098/rsta.2014.0071).
- Sørensen, J.N., Shen, W.Z., 2002. Numerical modeling of wind turbine wakes. *ASME Journal of Fluids Engineering* 124(2), 393 – 399. URL: <http://fluidsengineering.asmedigitalcollection.asme.org/article.aspx?articleid=1429525>, doi:[10.1115/1.1471361](https://doi.org/10.1115/1.1471361).
- Stanly, R., 2020. Large Eddy Simulation of Rotors: Filtered Actuator Line Modelling of Wind Turbines and Aeroacoustics of Propeller. Master's thesis Technion - Israel Institute of Technology.
- Stanly, R., Delorme, Y.T., Frankel, S.H., 2020. Computational Assessment of Actuator Line Model for Large Eddy Simulation of Rotor Noise. URL: <https://arc.aiaa.org/doi/abs/10.2514/6.2020-0035>, doi:[10.2514/6.2020-0035](https://doi.org/10.2514/6.2020-0035), [arXiv:https://arc.aiaa.org/doi/pdf/10.2514/6.2020-0035](https://arc.aiaa.org/doi/pdf/10.2514/6.2020-0035).
- Steijl, R., Barakos, G., 2008. Sliding mesh algorithm for cfd analysis of helicopter rotor–fuselage aerodynamics. *International Journal for Numerical Methods in Fluids* 58, 527–549. URL: <https://onlinelibrary.wiley.com/doi/abs/10.1002/flid.1757>, doi:[10.1002/flid.1757](https://doi.org/10.1002/flid.1757).
- Stevens, R.J., Martínez-Tossas, L.A., Meneveau, C., 2018. Comparison of wind farm large eddy simulations using actuator disk and actuator line models with wind tunnel experiments. *Renewable Energy* 116, 470 – 478. URL: <http://www.sciencedirect.com/science/article/pii/S0960148117308339>, doi:<https://doi.org/10.1016/j.renene.2017.08.072>.
- Storey, R.C., Norris, S.E., Cater, J.E., 2014. Modelling turbine loads during an extreme coherent gust using large eddy simulation. *Journal of Physics: Conference Series* 524, 012177. URL: <https://doi.org/10.1088/1742-6596/524/1/012177>, doi:[10.1088/1742-6596/524/1/012177](https://doi.org/10.1088/1742-6596/524/1/012177).
- Storey, R.C., Norris, S.E., Cater, J.E., 2015. An actuator sector method for efficient transient wind turbine simulation. *Wind Energy* 18, 699–711. URL: <https://onlinelibrary.wiley.com/doi/abs/10.1002/we.1722>, doi:<https://doi.org/10.1002/we.1722>.
- Strand, B., 1994. Summation by parts for finite difference approximations for d/dx. *Journal of Computational Physics* 110, 47 – 67. URL: <http://www.sciencedirect.com/science/article/pii/S0021999184710059>, doi:<https://doi.org/10.1006/jcph.1994.1005>.
- Sørensen, J.N., Myken, A., 1992. Unsteady actuator disc model for horizontal axis wind turbines. *Journal of Wind Engineering and Industrial Aerodynamics* 39, 139 – 149. URL: <http://www.sciencedirect.com/science/article/pii/016761059290540Q>, doi:[https://doi.org/10.1016/0167-6105\(92\)90540-Q](https://doi.org/10.1016/0167-6105(92)90540-Q).
- Troldborg, N., 2009. Actuator Line Modeling of Wind Turbine Wakes. Ph.D. thesis. Denmark Technical University.
- Troldborg, N., Larsen, G.C., Madsen, H.A., Hansen, K.S., Sørensen, J.N., Mikkelsen, R., 2011. Numerical simulations of wake interaction between two wind turbines at various inflow conditions. *Wind Energy* 14, 859–876. URL: <https://onlinelibrary.wiley.com/doi/abs/10.1002/we.433>, doi:<https://doi.org/10.1002/we.433>.
- Troldborg, N., Sørensen, J.N., Mikkelsen, R., Sørensen, N.N., 2014. A simple atmospheric boundary layer model applied to large eddy simulations of wind turbine wakes. *Wind Energy* 17, 657–669. URL: <https://onlinelibrary.wiley.com/doi/abs/10.1002/we.1608>, doi:<https://doi.org/10.1002/we.1608>.
- Troldborg, N., Sørensen, N., Réthoré, P.E., van der Laan, M., 2015a. A consistent method for finite volume discretization of body forces on collocated grids applied to flow through an actuator disk. *Computers & Fluids* 119, 197 – 203. URL: <http://www.sciencedirect.com/science/article/pii/S0045793015002194>, doi:<https://doi.org/10.1016/j.compfluid.2015.06.028>.
- Troldborg, N., Zahle, F., Réthoré, P.E., Sørensen, N.N., 2015b. Comparison of wind turbine wake properties in non-sheared inflow predicted by different computational fluid dynamics rotor models. *Wind Energy* 18, 1239–1250. URL: <https://onlinelibrary.wiley.com/doi/abs/10.1002/we.1757>, doi:<https://doi.org/10.1002/we.1757>.
- Vasurato, R., Kalkman, I., Blocken, B., van Wesemael, P., 2018. Large eddy simulation of the neutral atmospheric boundary layer: performance evaluation of three inflow methods for terrains with different roughness. *Journal of Wind Engineering and Industrial Aerodynamics* 173, 241–261. URL: <https://www.sciencedirect.com/science/article/pii/S0167610517300168>, doi:<https://doi.org/10.1016/j.jweia.2017.11.025>.
- Wasala, S.H., Storey, R.C., Norris, S.E., Cater, J.E., 2015. Aeroacoustic noise prediction for wind turbines using large eddy simulation. *Journal of Wind Engineering and Industrial Aerodynamics* 145, 17 – 29. URL: <http://www.sciencedirect.com/science/article/pii/S0167610515001336>, doi:<https://doi.org/10.1016/j.jweia.2015.05.011>.
- Yan, J., Deng, X., Korobenko, A., Bazilevs, Y., 2017. Free-surface flow modeling and simulation of horizontal-axis tidal-stream turbines. *Computers & Fluids* 158, 157 – 166. URL: <http://www.sciencedirect.com/science/article/pii/S0045793016302018>, doi:<https://doi.org/10.1016/j.compfluid.2016.06.016>. large-eddy and direct numerical simulations of oceanic and atmospheric flows.
- Yan, J., Korobenko, A., Deng, X., Bazilevs, Y., 2016. Computational free-surface fluid–structure interaction with application to floating offshore wind turbines. *Computers & Fluids* 141, 155 – 174. URL: <http://www.sciencedirect.com/science/article/pii/S0045793016300536>, doi:<https://doi.org/10.1016/j.compfluid.2016.03.008>. ad-

1210 vances in Fluid-Structure Interaction.
1211 Yang, X., Sotiropoulos, F., 2018. A new class of actuator surface mod-
1212 els for wind turbines. *Wind Energy* 21, 285–302. URL: <https://onlinelibrary.wiley.com/doi/abs/10.1002/we.2162>, doi:10.
1213 //onlinelibrary.wiley.com/doi/abs/10.1002/we.2162, doi:10.
1214 1002/we.2162.
1215 Zhong, W., Wang, T.G., Zhu, W.J., Shen, W.Z., 2019. Evaluation of tip loss
1216 corrections to ad/ns simulations of wind turbine aerodynamic performance.
1217 *Applied Sciences* 9. URL: [https://www.mdpi.com/2076-3417/9/22/](https://www.mdpi.com/2076-3417/9/22/4919)
1218 4919, doi:10.3390/app9224919.
1219 Önder, A., Meyers, J., 2018. On the interaction of very-large-scale motions in
1220 a neutral atmospheric boundary layer with a row of wind turbines. *Journal*
1221 *of Fluid Mechanics* 841, 1040–1072. doi:10.1017/jfm.2018.86.